Chaos in the Double Pendulum

SUNY Polytechnic Institute

MAT460 Numerical Differential Equations

Spring 2017

Christopher Indolfi

Douglas Nedza

5/5/2017

Contents

List of Figures

The goal of solving any differential equation is to be able to accurately predict the behavior of the system at any given time. This project attempts to accurately model the position of a double pendulum over time for a range of initial conditions. While seemingly a simple task, the double pendulum system displays chaotic behavior such that small variations between two initial conditions can lead to large discrepancies over time. The difficulty of analyzing a model of this system is increased by the lack of an analytic solution to the problem. Without a known solution to compare to, determining the error of discrete simulations is more complicated than simply finding the difference.

Employing a computer to solve differential equations requires that a numerical method be chosen that is able to discretely calculate values for a continuous differential equation. Some error is always expected with evaluating a continuous function in a discrete manner; however, the error of individual methods varies widely and the criteria for choosing the best method must be carefully considered.

To determine error in most cases, the numerical solution is compared to the analytic solution with the difference between them representing the error of the numerical method. Without an analytic solution to the differential system, error analysis of numerical methods is limited in scope. Numerical methods can be compared to each other to determine the error between them, and a novel technique known as backwards error analysis can be used to determine how far from the original initial conditions the computed numerical solution's initial conditions stray.

While the analysis of numerical methods is valuable, the more interesting portion of this project is the investigation of the chaotic behavior of this differential system. Questions we seek to answer are: how is a system determined to be chaotic? Is a system always chaotic/at what point does it become chaotic? After attempting to answer these questions a parameter sweep is performed on the double pendulum system to show how chaotic behavior changes as the system is altered.

1 Modeling

The subject of this study is the double penedulum depcited in Figure 1. It consists of a sequence of connected rods and masses that is attached at one end to a fixed pivot joint. The masses are assumed to be well approximated as point masses, the rods are assumed to be massless, and the pivot joint is assumed to be frictionless. The system is allowed to swing freely in a gravitational field pointing downward. In particular, the mass in the bottom arm, m_2, is not obstructed by the rod in the top arm. It can trace out a complete circle centered at mass m_1 without changing direction.

There are various ways of deriving the equations of motion for this system. Newtonian mechanics analyzes the problem using forces, positions, and velocities that are naturally described using a global coordinate system. Simply drawing the requisite free body diagrams, accounting for all the forces, and applying Newton's second law of motion will result in an underdetermined system of equations. This stems from the fact that double pendulum has four degrees of freedom and is completely described by the variables θ_1, θ_2, $\dot{\theta}_1$, and $\dot{\theta}_3$. An analysis couched within a Cartesian or polar coordinate system describes the system using eight quantities, namely the components of the position and velocity vectors for each mass. One way around this problem is to impose additional constraints like $l_1^2 = x_1^2 + y_1^2$

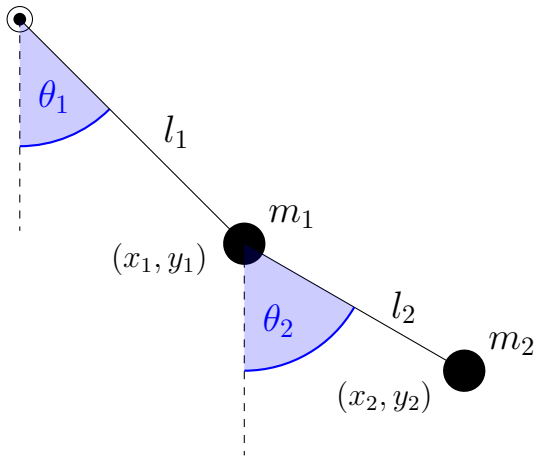

Figure 1: Double Pendulum

and $l_2^2 = (x_2 - x_1)^2 + (y_2 - y_1)^2$. Two additional constraints are needed to reduce the degrees of freedom to four. This method will certainly work, but for the double pendulum it is analytically obtuse and for pendula with more masses it quickly become untenable. Instead, we opted for the energy based approach offered by Hamiltonian mechanics.

1.1 Hamiltonian Systems

Phenomena from molecular dynamics, classical mechanics, quantum mechanics, fluid dynamics, image processing, and many more are described by ODEs that constitute a Hamiltonian system. Systems of this variety are entirely characterized by a single scalar function H, called the Hamiltonian, which takes two vector arguments: the canonical positions $\boldsymbol{q}$ and the canonical congujate momenta $\boldsymbol{p}$. The equations of motion are given by Hamilton's equations

$$\dot{\boldsymbol{q}} = \nabla_p \mathcal{H}(\boldsymbol{p}, \boldsymbol{q}), \qquad \dot{\boldsymbol{p}} = -\nabla_q \mathcal{H}(\boldsymbol{p}, \boldsymbol{q})\,. \tag{1}$$

If we let

$$\boldsymbol{y} = \begin{bmatrix} \boldsymbol{p} \\ \boldsymbol{q} \end{bmatrix} \qquad \text{and} \qquad \boldsymbol{J} = \begin{bmatrix} \boldsymbol{0} & \boldsymbol{I} \\ -\boldsymbol{I} & \boldsymbol{0} \end{bmatrix},$$

then these equations can be alternatively written as

$$\dot{\boldsymbol{y}} = \boldsymbol{J}^{-1} \nabla \mathcal{H}(\boldsymbol{y})\,.$$

Canonical coordinates are a set of parameters that describe a system at any point in time which satisfy

$$\{q_i, q_j\} = 0, \qquad \{p_i, p_j\} = 0, \qquad \{q_i, p_j\} = \delta_{ij},$$

where $\{\cdot, \cdot\}$ is the Poisson bracket and δ_{ij} is the Kronecker delta. Generalized coordinates are an alternative, albeit related, way of parameterizing the model that describe the configuration of the system relative to a reference configuration. The generalized velocities are

defined to be the time derivative of the generalized coordinates. In terms of position, the generalized and canonical formulations are equivalent. Concretely, both the canonical positions and generalized coordinates in Figure 1 are θ_1 and θ_2, the generalized velocities are $\dot{\theta}_1$ and $\dot{\theta}_2$, and the canonical congujate momenta p_1 and p_2 are related to, but distinct from, $\dot{\theta}_1$ and $\dot{\theta}_2$, respectively. Transforming the velocties into the momenta requires an understanding of the relationship between Hamilton's approach and that of his French contemporary Lagrange.

Lagrangian mechanics is a reformulation of Newtonian mechanics and served as the precursor to Hamilton's formulation. The theory uses generalized coordinates and characterizes the system's dynamics by a single scalar function called the Lagrangian, denoted $\mathcal{L}$. Within the domain of classical mechanics, the Lagrangian is known to be the difference between kinetic energy T and the potential energy U,

$$\mathcal{L} = T - U\,. \tag{2}$$

The Hamiltonian and Lagrangian formulations are related by the Legendre transform

$$p_i = \frac{\partial \mathcal{L}}{\partial \dot{\theta}_i} \qquad \mathcal{H} = \sum p_i \theta_i - \mathcal{L}\,. \tag{3}$$

Under this transformation, the Hamiltonian of a mechanical system is found to be equivalent to the total energy of the system. That is, it is equal to the sum of all kinetic and potential energies.

1.1.1 Properties of Hamiltonian Systems

There are two properties of Hamiltonian systems that play a central role in the numerical analysis undertaken here. The first of these is presented in the following proposition.

Proposition 1. *The Hamiltonian is invariant along solution trajectories,*

$$\dot{\mathcal{H}} = 0$$

Proof.

$$\dot{\mathcal{H}} = \frac{\partial \mathcal{H}}{\partial q}\dot{\boldsymbol{q}} + \frac{\partial \mathcal{H}}{\partial p}\dot{\boldsymbol{p}} = \dot{\boldsymbol{p}}\dot{\boldsymbol{q}} - \dot{\boldsymbol{q}}\dot{\boldsymbol{p}} = 0$$

□

In light of the fact that the Hamiltonian of a mechanical system is equivalent to the total energy in that system, proposition 1 is simply a reflection of the physical law of conservation of energy.

A large class of Hamiltonian systems are endowed with a special geometric structure; they are symplectic. In short, symplecticity in the current context means that the total area of regions in phase space is preserved as the system evolves forward in time. But, to be more precise we first define what a linear symplectic map is.

Definition 1. *A linear map, whose associated matrix is* $\boldsymbol{A}$*, is said to be symplectic if*

$$\boldsymbol{A}^T \boldsymbol{J} \boldsymbol{A} = \boldsymbol{J}$$

where

$$\boldsymbol{J} = \begin{bmatrix} \mathbf{0} & \boldsymbol{I} \\ -\boldsymbol{I} & \mathbf{0} \end{bmatrix}$$

Since $\boldsymbol{J}$ is a block matrix whose component matrices all commute with each other, it can be shown that the determinat of $\boldsymbol{J}$ is given by

$$\det \boldsymbol{J} = \det(\mathbf{00} - -\boldsymbol{I}\boldsymbol{I}) = \det \boldsymbol{I} = 1\,.$$

Therefore, given a matrix $\boldsymbol{A}$ which defines a linear symplectic transform,

$$\begin{aligned} \det\left(\boldsymbol{A}^T \boldsymbol{J} \boldsymbol{A}\right) &= \det \boldsymbol{J} \\ (\det \boldsymbol{A}^T)(\det \boldsymbol{J})(\det \boldsymbol{A}) &= 1 \\ (\det \boldsymbol{A}^T)(\det \boldsymbol{A}) &= 1 \\ (\det \boldsymbol{A})^2 &= 1 \\ \det \boldsymbol{A} &= \pm 1\,. \end{aligned}$$

Consequently, symplectic linear maps preserve volume. Next we extend the definition to a differentiable functions.

Definition 2. *A differentiable function* $\boldsymbol{\varphi} : \Omega \subset \mathbb{R}^{2d} \to \mathbb{R}^{2d}$ *is said to be sympletic if its Jacobian matrix is everywhere sympletic*

$$\nabla \boldsymbol{\varphi}^T \boldsymbol{J} \nabla \boldsymbol{\varphi} = \boldsymbol{J} \qquad \textit{for all } \boldsymbol{y} \in \Omega$$

Up to this point, symplecticity has been defined in a general setting. In order to understand its relevance to Hamiltonian systems we must first define the flow map $\boldsymbol{\varphi}_t(\boldsymbol{y}_0)$.

Definition 3. *For an autonomous ordinary differential equation* $\dot{\boldsymbol{y}} = f(\boldsymbol{y})$ *where* $\boldsymbol{y} \in \mathbb{R}^d$*, the flow map* $\boldsymbol{\varphi}_t(\boldsymbol{y}_0) : \mathbb{R}^{2d} \to \mathbb{R}^{2d}$ *takes the initial condition* $\boldsymbol{y}_0$ *to the value* $\boldsymbol{y}(t)$*,*

$$\boldsymbol{\varphi}_t(\boldsymbol{y}_0) = \boldsymbol{y}(t)$$

The definition of the flow map can be extended to apply to measurable sets with nonzero measure. That is, in addition to the single vector $\boldsymbol{y}_0$, one can also flow regions of well-defined volume through phase space. Given a set of initial conditions $\Omega \subset \mathbb{R}^{2d}$ the flow of that set is

$$\boldsymbol{\varphi}_t(\Omega) = \{\boldsymbol{y}(t) \mid \text{for all } \boldsymbol{y}_0 \in \Omega\}\,.$$

Consider a set $\Omega \subset \mathbb{R}^{2d}$ of in phase space which is evolved forward in time. Next, construct the sets Ω_k by projecting Ω onto each of the congujate (p_k, q_k)-planes,

$$\Omega_k = \left\{ \begin{bmatrix} \omega_k \\ \omega_{k+d} \end{bmatrix} \;\middle|\; \forall \boldsymbol{\omega} \in \Omega \right\} \qquad k = 1, ..., d\,.$$

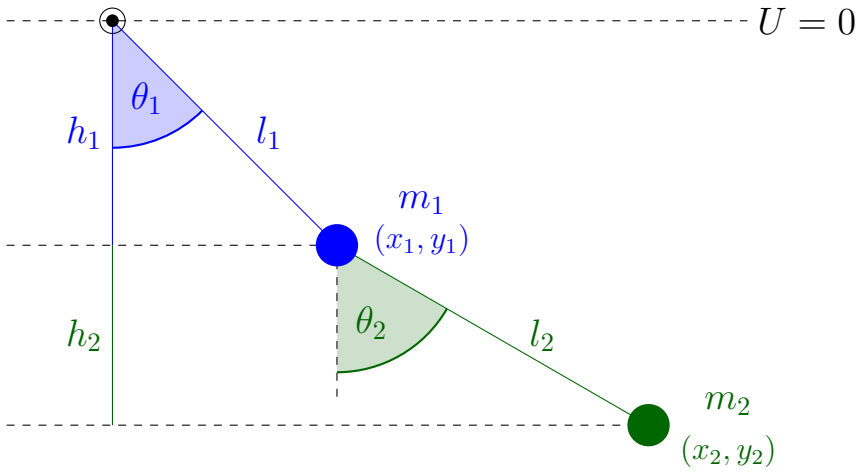

Figure 2: Double Pendulum

The symplectic property goes beyond volume preserving and implies that the sum of the oriented (i.e. signed) area of each of these sets,

$$\text{area}(\Omega_1) + \text{area}(\Omega_2) + \cdots + \text{area}(\Omega_k) \tag{4}$$

is invariant as the region Ω flows through phase space. In other words, for any measureable set of initial conditions whose measure is nonzero, the area of the projection onto any single congujate plane will vary as the system evolves, but the combined signed area of all projections will remain constant. Not every Hamiltonian system enjoys this property, but fortuantley a large class of systems do and the requisite condition is given in the following theorem attributed to Poincare.

Theorem 1. *If $\mathcal{H}$ is twice continuously differentiable, then the corresponding flow map $\boldsymbol{\varphi}_t(\boldsymbol{y}_0)$ is symplectic.*

1.2 Double Pendulum

The equations governing the double pendulum shown in Figure 2 are derived by turning Hamilton's crank: define the Lagrangian in terms of the kinetic and potential energy, apply the Legendre transform to get the Hamiltonian, and then evaluate Hamilton's equations to get the equations of motion.

1.2.1 Lagrangian

The potential energy of a mass is taken to be zero when the vertical displacement between the mass and the pivot joint is zero. Therefore, the potential energy of each mass is,

$$\begin{aligned} U_1 &= -m_1 h_1 g = m_1 l_1 g \cos\theta_1 \\ U_2 &= m_2(h_1 + h_2)g = m_2 g(l_1 \cos\theta_1 + l_2 \cos\theta_2), \end{aligned}$$

and the total potential energy is

$$U = U_1 + U_2 = -l_1(m_1 + m_2)g\cos\theta_1 - l_2 m_2 g\cos\theta_2\,. \tag{5}$$

The kinetic energy of a mass is $T = 1/2mv^2$, where v is the linear speed of the mass. The speed of the first mass, v_1, is easily obtained in terms of the generalized velocity $\dot{\theta}_1$,

$$T_1 = \frac{1}{2}m_1 v_1^2 = \frac{1}{2}m_1(l_1\dot{\theta}_1)^2 = \frac{1}{2}m_1 l_1^2\dot{\theta}_1^2\,.$$

Finding the speed of the second mass is slightly more involved. After writing the position of m_2 in a Cartesian coordinate system located at the pivot joint,

$$\begin{aligned} x_2 &= l_1\sin\theta_1 + l_2\sin\theta_2 \\ y_2 &= l_1\cos\theta_1 + l_2\cos\theta_2 \end{aligned}$$

the linear velocity is calculated by differentiating with respect to time,

$$\boldsymbol{v}_2 = \begin{bmatrix}\dot{x}_2\\ \dot{y}_2\end{bmatrix} = \begin{bmatrix} l_1\cos\theta_1 & l_2\cos\theta_2 \\ -l_1\sin\theta_1 & -l_2\sin\theta_2\end{bmatrix}\begin{bmatrix}\dot{\theta}_1\\ \dot{\theta}_2\end{bmatrix}\,.$$

With the velocity in hand, the kinetic energy of the second mass is

$$\begin{aligned} T_2 &= \frac{1}{2}\boldsymbol{v}_2^T\begin{bmatrix}m_2 & 0\\ 0 & m_2\end{bmatrix}\boldsymbol{v}_2 \\ &= \frac{1}{2}\begin{bmatrix}\dot{\theta}_1 & \dot{\theta}_2\end{bmatrix}\begin{bmatrix} l_1\cos\theta_1 & -l_1\sin\theta_1 \\ l_2\cos\theta_2 & -l_2\sin\theta_2\end{bmatrix}\begin{bmatrix}m_2 & 0\\ 0 & m_2\end{bmatrix}\begin{bmatrix} l_1\cos\theta_1 & l_2\cos\theta_2 \\ -l_1\sin\theta_1 & -l_2\sin\theta_2\end{bmatrix}\begin{bmatrix}\dot{\theta}_1\\ \dot{\theta}_2\end{bmatrix} \\ &= \frac{1}{2}m_2\left[l_1^2\dot{\theta}_1^2 + 2l_1l_2\cos(\theta_1-\theta_2)\dot{\theta}_1\dot{\theta}_2 + l_2^2\dot{\theta}_2^2\right]\,. \end{aligned}$$

So, the total kinetic energy is

$$T = T_1 + T_2 = \frac{1}{2}\left[l_1^2(m_1+m_2)\dot{\theta}_1^2 + 2l_1l_2m_2\cos(\theta_1-\theta_2)\dot{\theta}_1\dot{\theta}_2 + l_2^2m_2\dot{\theta}_2^2\right]\,. \tag{6}$$

To arrive at the Lagrangian for the double pendulum, all that remains to be done is to substitute equations (5) and (6) into the general form of the Lagrangian given by equation (2),

$$\begin{aligned} \mathcal{L} = &\frac{1}{2}\left[l_1^2(m_1+m_2)\dot{\theta}_1^2 + 2l_1l_2m_2\cos(\theta_1-\theta_2)\dot{\theta}_1\dot{\theta}_2 + l_2^2m_2\dot{\theta}_2^2\right] \\ &+ l_1(m_1+m_2)g\cos\theta_1 + l_2m_2g\cos\theta_2\,. \end{aligned}$$

1.2.2 Hamiltonian

Next, the Legendre transform in equation (3) is used to compute the canonical congujate momenta and the Hamiltonian. The momenta are

$$\begin{aligned} p_1 &= \frac{\partial\mathcal{L}}{\partial\dot{\theta}_1} = l_1^2(m_1+m_2)\dot{\theta}_1 + l_1l_2m_2\cos(\theta_1-\theta_2)\dot{\theta}_2 \\ p_2 &= \frac{\partial\mathcal{L}}{\partial\dot{\theta}_2} = l_1l_2m_2\cos(\theta_1-\theta_2)\dot{\theta}_1 + l_2^2m_2\dot{\theta}_2 \end{aligned}$$

which can be written as the matrix equation

$$\boldsymbol{p} = \begin{bmatrix} p_1 \\ p_2 \end{bmatrix} = \begin{bmatrix} l_1^2(m_1+m_2) & l_1 l_2 m_2 \cos(\theta_1-\theta_2) \\ l_1 l_2 m_2 \cos(\theta_1-\theta_2) & l_2^2 m_2 \end{bmatrix} \begin{bmatrix} \dot{\theta}_1 \\ \dot{\theta}_2 \end{bmatrix} . \tag{7}$$

Similarly, the Legendre transform can be written in matrix notation as

$$\mathcal{H} = \boldsymbol{p}^T \dot{\boldsymbol{\theta}} - \mathcal{L} . \tag{8}$$

Evaluating the first term yields,

$$\boldsymbol{p}^T \dot{\boldsymbol{\theta}} = \begin{bmatrix} \dot{\theta}_1 & \dot{\theta}_2 \end{bmatrix} \begin{bmatrix} l_1^2(m_1+m_2) & l_1 l_2 m_2 \cos(\theta_1-\theta_2) \\ l_1 l_2 m_2 \cos(\theta_1-\theta_2) & l_2^2 m_2 \end{bmatrix} \begin{bmatrix} \dot{\theta}_1 \\ \dot{\theta}_2 \end{bmatrix}$$

$$\boldsymbol{p}^T \dot{\boldsymbol{\theta}} = l_1^2(m_1+m_2)\dot{\theta}_1^2 + 2 l_1 l_2 m_2 \cos(\theta_1-\theta_2)\dot{\theta}_1\dot{\theta}_2 + l_2^2 m_2 \dot{\theta}_2^2 \tag{9}$$

and after substituting equation (9) into equation (3) the Hamiltonian for the double pendulum is found to be

$$\mathcal{H} = \frac{1}{2}\left[l_1^2(m_1+m_2)\dot{\theta}_1^2 + 2 l_1 l_2 m_2 \cos(\theta_1-\theta_2)\dot{\theta}_1\dot{\theta}_2 + l_2^2 m_2 \dot{\theta}_2^2 \right] \tag{10}$$

$$- l_1(m_1+m_2) g \cos\theta_1 - l_2 m_2 g \cos\theta_2 . \tag{11}$$

We note that, as it should be, the Hamiltonian is nothing more than

$$\mathcal{H} = T + U .$$

At this stage $\mathcal{H}$ is expressed in terms of position $\boldsymbol{\theta}$ and velocity $\dot{\boldsymbol{\theta}}$. Our last task is to replace the velocities with the corresponding momenta by solving equation (7) for $\dot{\boldsymbol{\theta}}$ and then substituting into equation (10). For notational clarty let

$$A := l_1^2(m_1+m_2), \quad B := l_1 l_2 m_2 \cos(\theta_1-\theta_2), \quad \text{and} \quad C := l_2^2 m_2,$$

so that equation (7) can be written compactly as,

$$\begin{bmatrix} p_1 \\ p_2 \end{bmatrix} = \begin{bmatrix} A & B \\ B & C \end{bmatrix} \begin{bmatrix} \dot{\theta}_1 \\ \dot{\theta}_2 \end{bmatrix}$$

and equation (10) becomes,

$$\mathcal{H} = \frac{1}{2}\left(A\dot{\theta}_1^2 + 2B\dot{\theta}_1\dot{\theta}_2 + C\dot{\theta}_2^2 \right) - l_1(m_1+m_2) g \cos\theta_1 - l_2 m_2 g \cos\theta_2 .$$

Calculating $\dot{\boldsymbol{\theta}}$ amounts to a straightforward matrix inversion,

$$\begin{bmatrix} \dot{\theta}_1 \\ \dot{\theta}_2 \end{bmatrix} = \frac{1}{AC-B^2} \begin{bmatrix} C & -B \\ -B & A \end{bmatrix} \begin{bmatrix} p_1 \\ p_2 \end{bmatrix}$$

which after a bit of algebra evaluates to

$$\dot{\theta}_1 = \frac{l_2^2 m_2 p_1 - l_1 l_2 m_2 \cos(\theta_1 - \theta_2) p_2}{l_1^2 l_2^2 m_2 \left(m_1 - m_2 \sin^2(\theta_1 - \theta_2)\right)} \tag{12}$$

$$\dot{\theta}_2 = \frac{-l_1 l_2 m_2 \cos(\theta_1 - \theta_2) p_1 + l_1^2 (m_1 + m_2) p_2}{l_1^2 l_2^2 m_2 \left(m_1 - m_2 \sin^2(\theta_1 - \theta_2)\right)} \,. \tag{13}$$

Because the potential energy does not depend on $\dot{\boldsymbol{\theta}}$, the task of writing the Hamiltonian in terms of $\boldsymbol{p}$ is reduced to substituting equations (12) and (13) into the kinetic energy,

$$\begin{aligned} T &= \frac{1}{2}\left(A\dot{\theta}_1^2 + 2B\dot{\theta}_1\dot{\theta}_2 + C\dot{\theta}_2^2\right) \\ &= \frac{1}{2}\left(\frac{A(Cp_1 - Bp_2)^2 + 2B(Cp_1 - Bp_2)(-Bp_1 + Ap_2) + C(-Bp_1 + Ap_2)^2}{(AC - B^2)^2}\right) \\ &= \frac{1}{2}\left(\frac{C(AC - B^2)p_1^2 - 2B(AC - B^2)p_1 p_2 + A(AC - B^2)p_2^2}{(AC - B^2)^2}\right) \\ &= \frac{1}{2}\left(\frac{Cp_1^2 - 2Bp_1 p_2 + Ap_2^2}{AC - B^2}\right) . \end{aligned}$$

Finally, the kinetic energy expressed using the canonical momenta is

$$T = \frac{l_2^2 m_2 p_1^2 - 2 l_1 l_2 m_2 \cos(\theta_1 - \theta_2) p_1 p_2 + l_1^2 (m_1 + m_2) p_2^2}{2 l_1^2 l_2^2 m_2 (m_1 + m_2 \sin^2(\theta_1 - \theta_2))},$$

and the Hamiltonian for the double pendulum is

$$\begin{aligned} \mathcal{H}(\boldsymbol{p}, \boldsymbol{\theta}) = &\frac{l_2^2 m_2 p_1^2 - 2 l_1 l_2 m_2 \cos(\theta_1 - \theta_2) p_1 p_2 + l_1^2 (m_1 + m_2) p_2^2}{2 l_1^2 l_2^2 m_2 (m_1 + m_2 \sin^2(\theta_1 - \theta_2))} \\ &- l_1 (m_1 + m_2) g \cos\theta_1 - l_2 m_2 g \cos\theta_2 \end{aligned} \,. \tag{14}$$

1.2.3 Equations of Motion

The equations of motion for the double pendulum are found by a direct application of the Hamilton's equations

$$\dot{\boldsymbol{\theta}} = \nabla_p \mathcal{H}(\boldsymbol{p}, \boldsymbol{\theta}) \qquad \dot{\boldsymbol{p}} = -\nabla_\theta \mathcal{H}(\boldsymbol{p}, \boldsymbol{\theta}) \,.$$

Calculating $\dot{\boldsymbol{\theta}}$ is a straightforward affair and solving for $\dot{\boldsymbol{p}}$, while also straightforward, is a tedious excersise, the details of which are omitted.

$$\dot{\theta}_1 = \frac{\partial \mathcal{H}}{\partial p_1} = \frac{l_2^2 m_2 p_1 - l_1 l_2 m_2 \cos(\theta_1 - \theta_2) p_2}{l_1^2 l_2^2 m_2 (m_1 + m_2 \sin^2(\theta_1 - \theta_2))} \tag{15}$$

$$\dot{\theta}_2 = \frac{\partial \mathcal{H}}{\partial p_2} = \frac{l_1^2 (m_1 + m_2) p_2 - l_1 l_2 m_2 \cos(\theta_1 - \theta_2) p_1) p_2}{l_1^2 l_2^2 m_2 (m_1 + m_2 \sin^2(\theta_1 - \theta_2))} \tag{16}$$

$$\dot{p_1} = -\frac{\partial \mathcal{H}}{\partial \theta_1} = -l_1 (m_1 + m_2) g \sin\theta_1 - C_1 + C_2 \tag{17}$$

$$\dot{p_2} = -\frac{\partial \mathcal{H}}{\partial \theta_2} = -l_2 m_2 g \sin\theta_2 + C_1 - C_2 \tag{18}$$

where

$$C_1 = \frac{\sin(\theta_1 - \theta_2) p_1 p_2}{l_1 l_2 (m_1 + m_2 \sin^2(\theta_1 - \theta_2))}$$

and

$$C_2 = \frac{l_2^2 m_2 p_1^2 - l_1 l_2 m_2 \cos(\theta_1 - \theta_2) p_1 p_2 + l_1^2 (m_1 + m_2) p_2^2}{2 l_1^2 l_2^2 (m_1 + m_2 \sin^2(\theta_1 - \theta_2))^2} .$$

2 Numerical Methods

Many systems of ordinary differential equations are not completely integrable and can only be solved numerically. Consider the general initial value problem

$$\dot{\boldsymbol{y}} = f(t, \boldsymbol{y}),\ t \geq t_0 \qquad \boldsymbol{y}_0 = \boldsymbol{y}(t_0) . \tag{19}$$

The numerical methods described here compute an approximate solution $\boldsymbol{y}_n$ evaluated over a discrete set of times given by

$$t_{n+1} = t_n + h_n$$

where h_n is the step size. Unless otherwise stated, we will assume that the step size is constant and drop the subscript. The values of the numerical solution are denoted by $\boldsymbol{y}_n$ and are related to the exact solution by

$$\boldsymbol{y}_n = \boldsymbol{y}(t_n) + \boldsymbol{e}_n$$

where $\boldsymbol{e}_n$ is the local approximation error. We say that a numerical method is of order p if the local error of the solution it generates is on the order of h^{p+1}, or stated equivelently,

$$\boldsymbol{y}_n = \boldsymbol{y}(t_n) + O(h^{p+1}) .$$

2.1 Runge-Kutta Methods

The Runge-Kutta family of solvers occupies a central place in the field of numerical analysis. These methods take the natural approach of solving equation (19) by integrating $f(t, \boldsymbol{y})$ over a single time step from t_n to t_{n+1},

$$\boldsymbol{y}(t_{n+1}) = \int_{t_n}^{t_{n+1}} f(\tau, \boldsymbol{y})\, d\tau .$$

After translating by t_n and scaling by $h = t_{n+1} - t_n$ this is equivalently written as

$$\boldsymbol{y}(t_{n+1}) = \boldsymbol{y}(t_n) + h \int_0^1 f(t_n + h\tau, \boldsymbol{y}(t_n + h\tau))\, d\tau .$$

To make the move into the numerical domain, the next logical step is to replace the integration by a quadrature,

$$\boldsymbol{y}_{n+1} = \boldsymbol{y}_n + h \sum_{j=0}^{s} b_j f(t_n + h c_j, \boldsymbol{y}(t_n + h c_j))$$

where $b_1, b_2, ..., b_s$ are called weights and $c_1, c_2, ..., c_s$ are nodes statisfying $0 \leq c_i \leq 1$. Despite giving a discrete solution, this formula is not applicable because $\boldsymbol{y}$ is unknown. To overcome this hurdle $\boldsymbol{y}$ must be approximated s times; these approximate solutions are denoted by k_j, where $j = 1, 2, ..., s$. To start, we take advantage of the fact that y_n is assumed to be known and set $c_1 = 0$ so that $k_1 = y_n$. For explicit methods, the i^{th} approximation is constructed as a linear combination of $f(t_n + hc_1, k_1)$, $f(t_n + hc_2, k_2)$, ..., $f(t_n + hc_j, k_j)$ for $j < i$:

$$\begin{aligned}
k_1 &= y_n \\
k_2 &= y_n + a_{21} f(t_n, k_1) \\
k_3 &= y_n + a_{31} f(t_n, k_1) + a_{32} f(t_n + hc_2, k_2) \\
&\vdots \\
k_\nu &= y_n + \sum_{i}^{s-1} a_{\nu i} f(t_n + hc_i, k_i) \\
y_{n+1} &= y_n + \sum_{j}^{s} b_j f(t_n + hc_j, k_j)\,.
\end{aligned}$$

Implicit Runge-Kutta methods generalize this structure by allowing each approximation k_i to be a linear combination over the set $\{\, f(t + hc_j, k_j) \mid j = 1, ..., s \,\}$. The general form of an s-stage Runge-Kutta method is

$$\begin{aligned}
k_1 &= f(t_n + hc_1,\, y_n + h(a_{11}k_1 + a_{12}k_2 + \cdots + a_{1s}k_s)) \\
k_2 &= f(t_n + hc_2,\, y_n + h(a_{21}k_1 + a_{22}k_2 + \cdots + a_{2s}k_s)) \\
&\vdots \\
k_s &= f(t_n + hc_s,\, y_n + h(a_{s1}k_1 + a_{s2}k_2 + \cdots + a_{ss}k_s))
\end{aligned}$$

$$y_{n+1} = y_n + h(b_1k_1 + b_2k_2 + \cdots + b_sk_s)\,.$$

This can be compactly represented by the Butcher table

$$\begin{array}{c|cccc}
c_1 & a_{11} & a_{12} & \cdots & a_{1s} \\
c_2 & a_{21} & a_{22} & \cdots & a_{2s} \\
\vdots & \vdots & & \ddots & \vdots \\
c_s & a_{s1} & a_{s2} & \cdots & a_{ss} \\
\hline
 & b_1 & b_2 & \cdots & b_4
\end{array}$$

2.2 Collocation Methods

Collocation methods are derived by choosing a set of nodes $c_1, c_2, ..., c_s$ within the unit interval and finding the polynomial of degree s that statisies the differential equation at each node as well as at the initial condition imposed by y_n. That is, the goal is to find a

polynomial $\boldsymbol{u}$ such that

$$\begin{aligned} \boldsymbol{u}(t_n) &= \boldsymbol{y}_n \\ \dot{\boldsymbol{u}}(t_n + hc_j) &= f(t_n + hc_j, \boldsymbol{u}(t_n + hc_j)) \qquad \text{for } j = 1, ..., s\,. \end{aligned}$$

With such a polynomial in hand, we simply set $\boldsymbol{y}_{n+1} = \boldsymbol{u}(t_{n+1})$. It can be shown that the collocation method just described can be cast in the Runge-Kutta framework by

$$a_{ij} = \int_0^{c_i} \frac{q_j(\tau)}{q_j(c_j)}\, d\tau, \qquad i, j = 1, 2, ..., s \tag{20}$$

$$b_j = \int_0^1 \frac{q_j(\tau)}{q_j(c_j)}\, d\tau, \qquad j = 1, 2, ..., s \tag{21}$$

where

$$q(t) = \prod_{j=1}^{s} (t - c_j) \quad \text{and} \quad q_k(t) = \frac{q(t)}{t - c_k}\,.$$

The Gauss-Legendre collocation methods are a specialization that will turn out to have a particular useful property. Let $\{P_1, P_2, ..., P_s\}$ be the set of polynomials that are orthogonal with respect to the weight function $\omega(t) = 1$ on the interval $t \in [0, 1]$. That is, they satisfy

$$\int_0^1 P_i(t) P_j(t)\, dt = 0 \qquad i, j = 1, ..., s \quad i \neq j\,.$$

The s-stage Gauss-Legendre collocation method is constructed by choosing $c_1, c_2, ..., c_s$ to be the zeros of P_s. The set $\{P_1, P_2, ..., P_s\}$ can be generated by linearly transforming the well known Legendre polynomials, which are orthogonal on the interval $t \in [-1, 1]$. Doing so yields

$$P_s(t) = \frac{(s!)^2}{(2s)!} \sum_{k=0}^{s} (-1)^{s-k} \binom{s}{k} \binom{s+k}{k} t^k\,. \tag{22}$$

It can be shown that an s-stage Gauss-Legendre method has an order of $2s$.

2.3 Sympletic Methods

Symplectic methods yield solutions to Hamiltonian systems that preserve their symplectic structure. That is, the symplectic area defined in equation (4) remains constant for all time. This is key to producing accurate, long-running simulations. The local approximation error of the energy for solutions resulting from symplectic methods is limited to $O(h^p)$. There exists no such guarantee for non-symplectic methods. Quite often symplectic methods produce solutions in which the energy oscillates around the exact value, whereas the energy of systems solved by non-symplectic techniques tends to increase or decrease as the system evolves. The near constant energy, at least taken on the average, does not last forever, but it will be maintained significantly longer than the energy of a solution which doesn't preserve the underlying geometric structure.

We state two theorems that can be used to determine if a particular numerical method is symplectic or not. The first of these gives a way to test whether a particular Runge-Kutta method is symplectic. The second is a stronger statement concerning an entire class of methods.

Theorem 2. *Given a Runge-Kutta method with Butcher table,*

$$\begin{array}{c|ccc} c_1 & a_{11} & \cdots & a_{1k} \\ \vdots & \vdots & \ddots & \vdots \\ c_k & a_{k1} & \cdots & a_{kk} \\ \hline & b_1 & \cdots & b_k \end{array}$$

Define the matrix $\boldsymbol{M}$ *to be,*

$$M_{ij} = b_i a_{ij} + b_j a_{ji} - b_i b_j$$

Then, if $\boldsymbol{M} = \boldsymbol{0}$ *the Runge-Kutta method is symplectic.*

Theorem 3. *Gauss-Legendre collocation methods are symplectic*

2.4 Specific Numerical Methods

2.4.1 Implicit Midpoint Rule

The implicit midpoint rule is the Gauss-Legendre collocation method corresponding to $s = 1$. As such, it is a second order symplectic method and, as its name implies, is implcit. According to equation (22),

$$P_1(t) = t - \frac{1}{2},$$

the zero of which is $c_1 = 1/2$. Using equations (20) and (21),

$$\begin{aligned} a_{11} &= \int_0^{1/2} d\tau = \frac{1}{2} \\ b_1 &= \int_0^1 d\tau = 1\,. \end{aligned}$$

Therefore the implicit midpoint rule is given by the butcher table

$$\begin{array}{c|c} 1/2 & 1/2 \\ \hline & 1 \end{array}$$

and the recursive formula,

$$\boldsymbol{y}_{n+1} = \boldsymbol{y}_n + hf\left(t_n + \frac{h}{2}, \frac{1}{2}\left(\boldsymbol{y}_n + \boldsymbol{y}_{n+1}\right)\right)\,. \tag{23}$$

2.4.2 Yoshida's Method

Various techniques have been developed to construct higher order solvers from lower order solvers. Composing multiple methods is one such approach. Yoshida's method is a fourth order implcit method constructed by composing three instances of the implicit midpoint method. First equation (23) is applied with a step size of αh, where $\alpha > 1$. That is followed by a backward step of size of $(2\alpha - 1)h$, and then a forward step of size αh. The sequence of temporal jumps finally lands on t_{n+1}. If α is chosen to be $1/(2 - \sqrt[3]{2})$ it can be shown that the method is symplectic. The algorithm is given by

$$\begin{aligned}
\boldsymbol{u}_1 &= \boldsymbol{y}_n + \alpha h f\left(t_n + \frac{\alpha h}{2},\ \frac{\boldsymbol{y}_n + \boldsymbol{u}_1}{2}\right) \\
\boldsymbol{u}_2 &= \boldsymbol{y}_n - (2\alpha - 1) h f\left(t_n - \frac{(\alpha - 1)h}{2},\ \frac{\boldsymbol{u}_1 + \boldsymbol{u}_2}{2}\right) \\
\boldsymbol{y}_{n+1} &= \boldsymbol{y}_n + \alpha h f\left(t_n + \frac{h}{2},\ \frac{u_2 + \boldsymbol{y}_{n+1}}{2}\right).
\end{aligned}$$

2.4.3 Forward Euler

Forward Euler is the perhaps the simplest approach that can be taken to numerically solve a differential equation. It is a first order explicit method whose Butcher table and recursive formula are

$$\begin{array}{c|c} 1 & 0 \\ \hline & 1 \end{array}$$

$$\boldsymbol{y}_{j+1} = \boldsymbol{y}_j + h_j f(t_j, \boldsymbol{y}_j)\,.$$

Theorem 2 can be used to test whether or not this method is symplectic. In this case the matrix $\boldsymbol{M}$ consists of a single entry,

$$M_{11} = b_1 a_{11} + b_1 a_{11} - b_1 b_1 = (1)(0) + (1)(0) - (1)(1) = -1\,.$$

Therefore, $\boldsymbol{M} \neq \boldsymbol{0}$ and forward Euler is not symplectic.

2.4.4 Classic Runge-Kutta

The classic fourth order Runge-Kutta method, refered to simply as *the* Runge-Kutta method, was developed by Runge and Kutta in 1900. It is an explicit scheme given by the following butcher table,

$$\begin{array}{c|cccc} 0 & & & & \\ 1/2 & 1/2 & & & \\ 1/2 & 0 & 1/2 & & \\ 0 & 0 & 0 & 1 & \\ \hline & 1/6 & 1/3 & 1/3 & 1/6 \end{array}$$

The solution is computed by the formula,

$$\begin{aligned} k_1 &= f\left(t_n,\, \boldsymbol{y}_n\right) \\ k_2 &= f\left(t_n + \frac{h}{2},\, \boldsymbol{y}_n + \frac{h}{2}k_1\right) \\ k_3 &= f\left(t_n + \frac{h}{2},\, \boldsymbol{y}_n + \frac{h}{2}k_2\right) \\ k_4 &= f\left(t_n + h,\, \boldsymbol{y}_n + hk_3\right) \end{aligned}$$

$$\boldsymbol{y}_{n+1} = \boldsymbol{y}_n + \frac{h}{6}\left(k_1 + 2k_2 + 2k_3 + k_4\right) .$$

Again, symplecticity is determined according to Theorem 2 by constructing the matrix $\boldsymbol{M}$,

$$\boldsymbol{M} = \frac{1}{6}\begin{bmatrix} 0 & 0 & 0 & 0 \\ 1 & 0 & 0 & 0 \\ 0 & 1 & 0 & 0 \\ 0 & 0 & 1 & 0 \end{bmatrix} + \frac{1}{6}\begin{bmatrix} 0 & 1/2 & 0 & 0 \\ 0 & 0 & 1 & 0 \\ 0 & 0 & 0 & 2 \\ 0 & 0 & 0 & 0 \end{bmatrix} - \frac{1}{36}\begin{bmatrix} 1 & 2 & 2 & 1 \\ 2 & 4 & 4 & 2 \\ 2 & 4 & 4 & 1 \\ 1 & 2 & 2 & 1 \end{bmatrix}$$

$$\boldsymbol{M} = \frac{1}{36}\begin{bmatrix} -1 & 1 & -2 & -1 \\ 4 & -4 & 2 & -2 \\ -2 & 2 & -4 & 11 \\ -1 & -2 & 4 & -1 \end{bmatrix} .$$

And, just like forward Euler, $\boldsymbol{M} \neq \boldsymbol{0}$ which implies that the classic Runge-Kutta method is not symplectic.

2.5 Error Analysis

In the absence of an analytical solution, direct calculation of the numerical error can not be acheived, and alternative methods of evaluating the quality of the approximation must be employed. The Hamiltonian can be evaluated exactly, and according to proposition 1 ought to remain constant for all time. As such, the difference between the energy computed at some arbitrary time $t > t_0$ and the energy evaluated at $t = t_0$ provides some measure of how well a numerical method solves a Hamiltonian system. Since fixing the energy reduces the number of free parameters in the equations of motion by one, the solution is restricted to a $(2d-1)$-dimensional subset of phase space. In the case of the double pendulum, the trajectories lie on a three-dimensional manifold in phase space. With this in mind, the error in energy can be interpreted as a measure of how close numerical solutions stay to the manifold containing the exact solution. This implies that solutions with small deviations in energy may still exhibit large error.

A second approach is to approximate the error of a numerical solution by comparing it with a second numerical solution obtained using a higher order method. This strategy will not provide an exact measure of error, but it does offer a estimate bounded by the following proposition.

Proposition 2. *Let $\dot{\boldsymbol{y}} = f(t, \boldsymbol{y})$ and $\boldsymbol{y}_0$ be an initial value problem. If $\boldsymbol{y}(t)$ is the exact solution, $\boldsymbol{y}_n$ is an approximate solution of order p, and $\tilde{\boldsymbol{y}}_n$ is an approximate solution of order $p+k$, where $k \geq 1$. Then $\|\tilde{\boldsymbol{y}}_n - \boldsymbol{y}_n\|$ is an approximation of the local error of $\boldsymbol{y}_n$. Moreover, the approximate error is of order $p+k$,*

$$\|\boldsymbol{y}(t_n) - \boldsymbol{y}_n\| = \|\tilde{\boldsymbol{y}}_n - \boldsymbol{y}_n\| + O(h^{p+k+1})\,.$$

Proof. Let $\boldsymbol{e}_n$ and $\tilde{\boldsymbol{e}}_n$ be the errors associated with the two approximate solutions such that,

$$\begin{aligned}\tilde{\boldsymbol{y}}_n &= \boldsymbol{y}(t_n) - \tilde{\boldsymbol{e}}_n \\ \boldsymbol{y}_n &= \boldsymbol{y}(t_n) - \boldsymbol{e}_n\,.\end{aligned}$$

Subtracting these two equations yields

$$\boldsymbol{e}_n = \tilde{\boldsymbol{y}}_n - \boldsymbol{y}_n + \tilde{\boldsymbol{e}}_n,$$

from which the result is readily obtained,

$$\|\boldsymbol{e}_n\| = \|\tilde{\boldsymbol{y}}_n - \boldsymbol{y}_n + \tilde{\boldsymbol{e}}_n\| \leq \|\tilde{\boldsymbol{y}}_n - \boldsymbol{y}_n\| + \|\tilde{\boldsymbol{e}}_n\| = \|\tilde{\boldsymbol{y}}_n - \boldsymbol{y}_n\| + O(h^{p+k+1})\,.$$

□

2.6 Poincare Map

The Poincare map transforms a $2d$-dimensional solution to a continuous time dynamical system into a $(2d-1)$-dimensional discrete dynamical system that can be used to study the properties of the continuous solution. It is constructed by considering the sequence of points at which the $2d$-dimensional orbits cross some arbitrary $2d-1$-dimensional oriented surface called the Poincare section. The orientation of the Poincare section divides phase space into two disjoint sets, let us call them the front and back sides of the surface. Only crossings that occur as the trajectory passes from the front to the back are included in the sequence. A formal definition is given below and a cartoon of the construction is shown in Figure 3.

Definition 4. *Given a solution $\boldsymbol{y}$ to the differential equation $\dot{\boldsymbol{y}} = f(t, \boldsymbol{y})$ choose some arbitrary $(2d-1)$-dimensional oriented surface in phase space to be the Poincare section S. Consider the sequence of times $\{t_k\}$ such that*

1. *$t_i < t_j$ for all $i < j$*
2. *$\boldsymbol{y}(t_i) \in S$*
3. *$\boldsymbol{y}(t_i^-)$ is on the front side of S*

The Poincare map P is defined to be

$$P(\boldsymbol{y}) = \{\boldsymbol{\rho_k}\} = \{\boldsymbol{y}(t_k)\}$$

The Poincare map encodes qualitative information about the solution $\boldsymbol{y}$. If $\boldsymbol{y}$ is periodic the sequence of points $\{\rho_k\}$ are also periodic. Consequently, the set of all points within that sequence is finite. Quasi-periodic motion is captured as a curve filling sequence whereas a chaotic trajectory produces an area filling sequence.

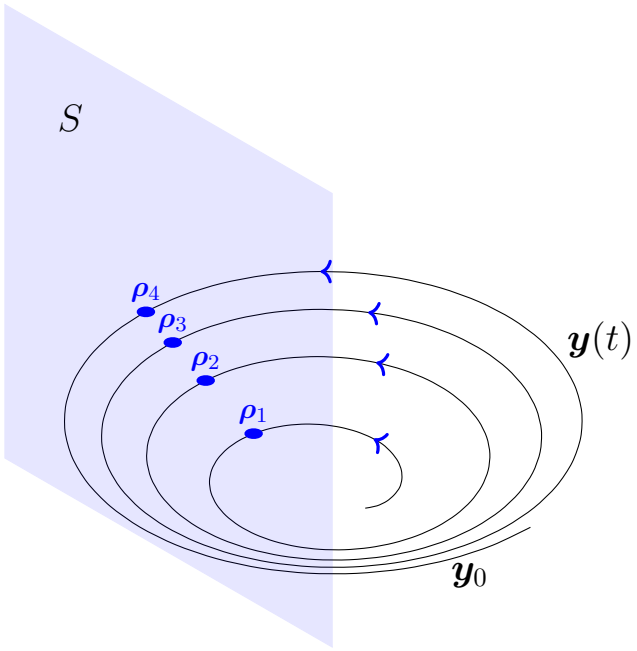

Figure 3: Construction of the Poincare map

3 Results

Our analysis is comprised of three parts. First, we simulated the motion of the double pendulum using two different initial conditions to compare the regular motion from chaotic motion. Secondly, we undertook an error analysis that compared the accuracy of the four methods identified above. Finally, the relationship between energy and the type of motion exhibited by the double pendulum was investigated through the use of Poincare sections. All of the experiments were conducted with the following parameters.

$$m_1 = 1, \quad m_2 = 3, \quad l_1 = 1, \quad l_2 = 2, \quad g = 1$$

3.1 Double Pendulum Simulation

It is well known that the double pendulum exhibits chaotic behavior, but this does not mean that the dynamics are chaotic for every initial condition. To qualitativly investigate the differences between regular and chaotic motion, the equations governing the double pendulum (equations (15) to (18)) were solved using the Yoshida method with $h = 0.01$ for $0 \leq t \leq 240$ seconds. This was done using two different initial conditions which varied only in θ_1; all other coordinates were started at zero. The first is $\boldsymbol{y}_0 = (0.8, 0, 0, 0)$, which results in quasiperiodic motion. The second solution is initially $\boldsymbol{y}_0 = (3, 0, 0, 0)$ and exhibits chaotic motion.

The time evolution of each simulation is plotted as a sequence of snap shots in Figure 4 and Figure 10. The blue curves show the path traced out by the second mass as the system evolved.

A second set of visualizations, presented in Figure 5 for the regular case and Figure 11 for the chaotic case, projects the phase space trajectory onto four axis-planes. Starting with the upper left plot and moving clockwise, the solution is projected onto the (θ_1, p_1)-plane, the (θ_2, p_2)-plane, the (p_1, p_2)-plane, and the (θ_1, θ_2)-plane. Regarding the regular behavior shown in Figure (5, it is interesting to note that the projections onto the congujate pair planes have a roughly circular appearance, while the projections onto the position and momenta planes in the bottom row show a somewhat rectangular envelope. The reason for this difference is made a bit more clear by Figures 6 to 9 and Figures 12 to 15 which contain pictures of phase space projected onto several three-dimensional subspaces. Each figure shows four views of the trajectory projected onto a three-dimensional subspace, plotted in blue, as well as the projections onto each of the axis planes, displayed in green, red, and cyan.

3.2 Error Analysis

An analysis of the quality of the numerical solutions obtained using the Yoshida method, the implicit midpoint method, the forward Euler method, and the classic Runge-Kutta method was taken up next. The equations of motion (15) to (18) were solved by all four methods using a step size of $h = 0.01$ and over a period of $T = 4200$ seconds. This was done, exactly like the previous experiment, over the set initial conditions $\boldsymbol{y}_0 = (0.8, 0, 0, 0)$ and $\boldsymbol{y}_0 = (3, 0, 0, 0)$.

The first measure that was considered was the deviation of the energy over the course of the simulation. The actual error in the energy along with a trend line is plotted over the entire 4200 seconds in Figures 17 and 19. The first 240 seconds are shown in Figures 16 and 18. When viewing these graphs it is important to take note of the scale on the $\Delta\mathcal{H}$ axis. At first glance the results for Yoshida's method and the implicit midpoint method look similar, but a careful reading shows that the two actually differ by four orders of magnitude. It should be noted the experiments in previous section correspond exactly with the results for the Yoshida's method in Figures 16 and 18, thereby offering one more point of comparison for the simulations run in the previous section.

Not suprisingly, Figure 16 shows that the solution using Euler's method grows linearly over the first 240 seconds. Nonetheless, in both the quasiperiodic and chaotic cases this does not continue but, loosely speaking, turns into a spiking pattern riding on top of a nearly constant trend. Both of the symplectic methods show a characteristic oscillating behavior. Still though, the trend lines for the regular motion are both slightly offset above zero. Also performing as expected, the Runge-Kutta solution shows nearly linear loss of energy as time progresses. Comparison of Figure 16 and Figure 18 show that the maximum ΔH using Yoshida's method increased by four orders of magnitude between the regular and chaotic cases. Similar differences are seen with respect to the implicit midpoint method, Euler's method, and the Runge-Kutta method. It is not clear whether these differences are due the chaotic motion or if they are simply a result of starting the system with a larger initial energy.

The time evolution of the system solved by each of the four methods is shown in Figures 24, 25, 26, and 27. The first 240 seconds and the entire 4200 seconds of the quasiperiodic case are shown Figures 24 and 25. Similarly, the first 90 seconds and 240 seconds of chaotic

motion are shown in Figures 26 and 27. Each frame shows four pendula colored blue, green, red, and orange which correspond to Yoshida's method, the implicit midpoint method, Euler's method, and the Runge-Kutta method, respectively. The curves show the path traced by the second mass for the six seconds leading up to the snap shot. Because each pendulum was started with the same initial condition, the pendula are stacked on top of each other in the first frame. As time progresses the solutions deviate and the pendula separate. All of these figures show that the solution using Euler's method significantly deviates from the other three almost immediatley. On the other hand, those three solutions stay consistent for the enirity of the quasiperiodic case. The chaotic solutions show that good agreement until around 50 seconds when the implicit midpoint pendulum becomes visible. By the 80 second mark none of the solutions are in agreement.

Lastly, we calculated the approximate error of the solution produced by the implicit midpoint method and the solution given by Euler's method. According to the prescription in proposition 2, the L^∞ distance between each of these solutions and the exact solution is approximately equal to difference between each solution and the solution resulting from Yoshida's method.

$$\boldsymbol{e}_{imp\,mid} \approx \|\boldsymbol{y}_{yoshida} - \boldsymbol{y}_{imp\,mid}\|_\infty$$
$$\boldsymbol{e}_{euler} \approx \|\boldsymbol{y}_{yoshida} - \boldsymbol{y}_{euler}\|_\infty$$

The results are shown in Figures 20, 21, 22, and 23. In addition, we also plotted the difference between the solutions from the two fourth order methods. It appears that the numerical results obtained for the regular behavior are consistent with the theory outlined in the methods section. The error between the chaotic solutions was not so well behaved. This is a consequence of the sensitivity of chaotic systems to differences in initial conditions. Even the smallest of errors incurred due to finite machine precision will be magnified exponentially until the numerical solution significantly deviates from the exact solution.

3.3 Poincare Maps

We know from the previous experiments that there is some correspondance between energy and the qualitative nature of the solution. To further investigate this phenomenon we constructed Poincare maps at the four different energy levels in the set $E = \{-8.5, -7.1, -6.9, -6.5\}$. The smallest of these is marginally larger than the minimum energy of -9 found by evaluating $\mathcal{H}$ at $\boldsymbol{y} = (0, 0, 0, 0)$. The chosen Poincare section is the hyperplane corresponding to the condition that $\theta_1 = 0$ and oriented so that only points where $p_1 > 0$ are kept. For each fixed energy $e \in E$, a set of initial conditions $\Omega \in \mathbb{R}^{2d}$ was calculated such that $\mathcal{H}(\boldsymbol{y}_0) = e$, for each $\boldsymbol{y}_0 \in \Omega$. Then, the Poincare map was computed for each $\boldsymbol{y}_0 \in \Omega$ and plotted using a color corresponding to the potential energy of $\boldsymbol{y}_0$. The resulting plots are presented in Figures 28 to 31. The lowest energy plot contains only line filling sequences which indicates that all the initial conditions chosen whose energy is -8.5 result in quasiperiodic motion. As the energy increases these curves deform and some of them bifurcate into an area filling set, indicating that those initial conditions lead to chaotic motion.

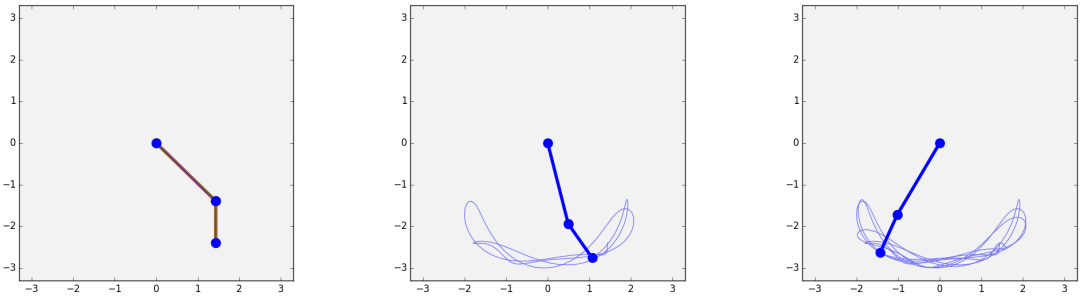

(a) $t = 0$ (b) $t = 21.77$ (c) $t = 43.61$

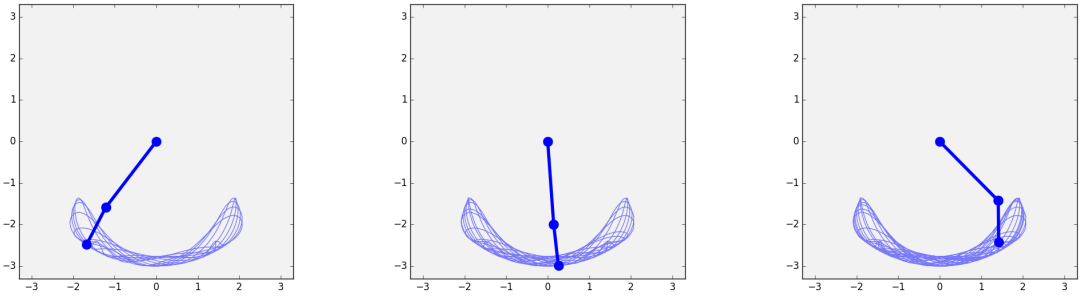

(d) $t = 65.45$ (e) $t = 87.22$ (f) $t = 109.06$

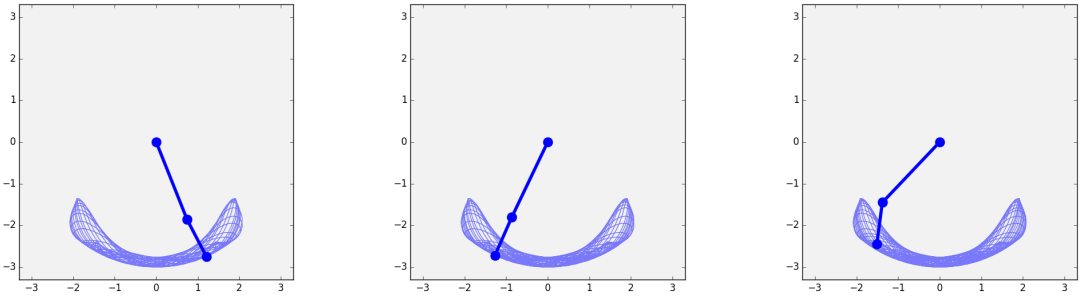

(g) $t = 130.9$ (h) $t = 152.74$ (i) $t = 174.51$

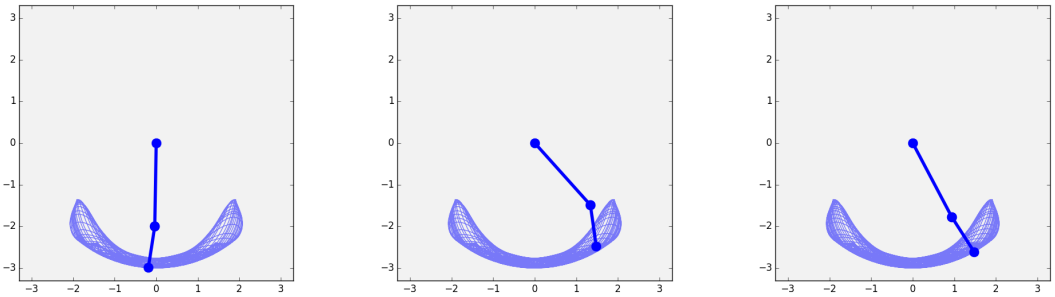

(j) $t = 196.35$ (k) $t = 218.19$ (l) $t = 240$

Figure 4: Quasiperiodic Motion - Time Evolution ($T = 240$ seconds)

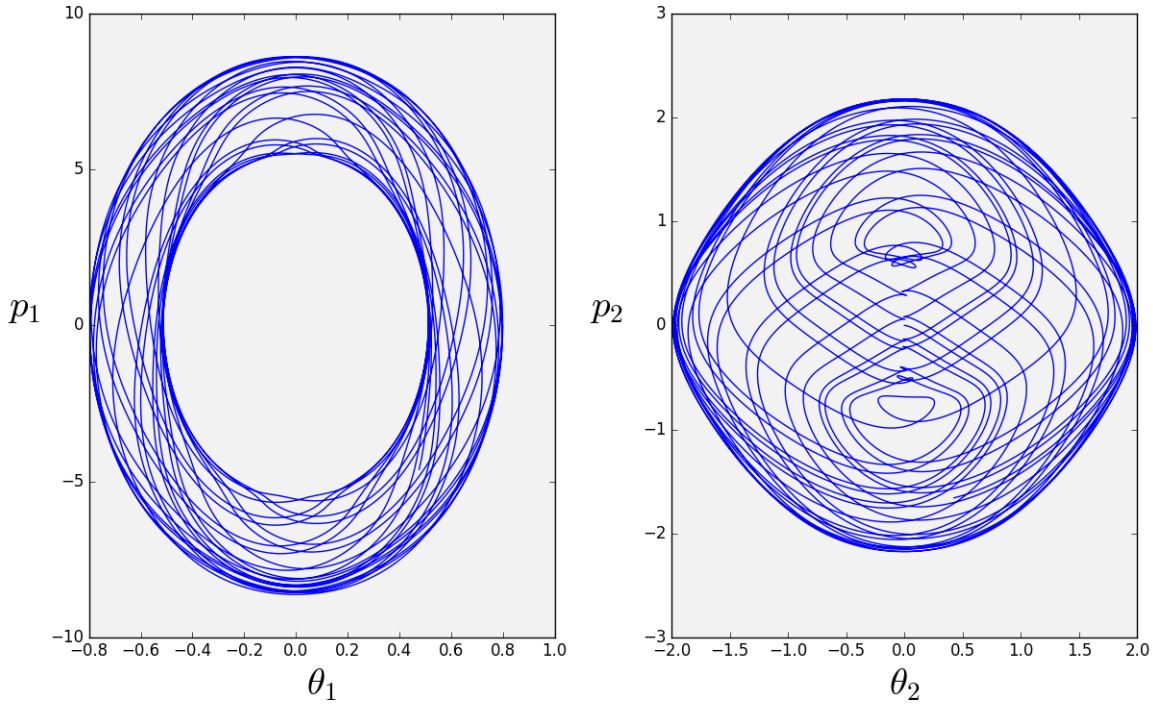

(a) θ_1 vs p_1

(b) θ_2 vs p_2

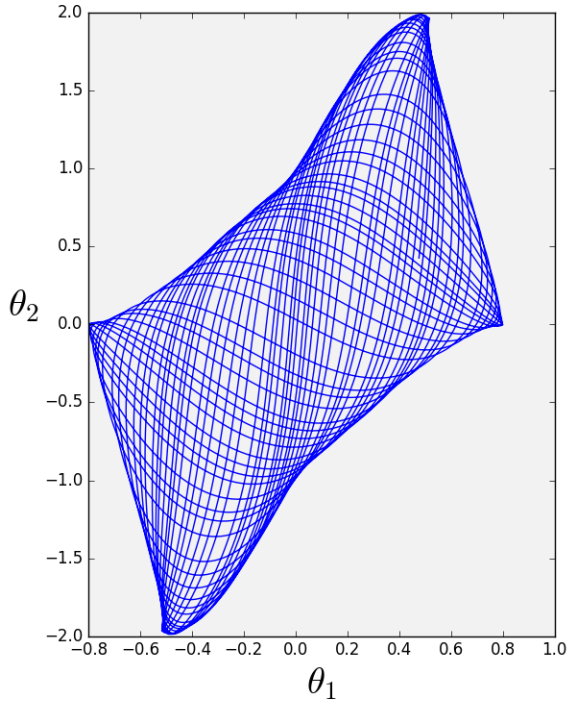

(c) θ_1 vs θ_2

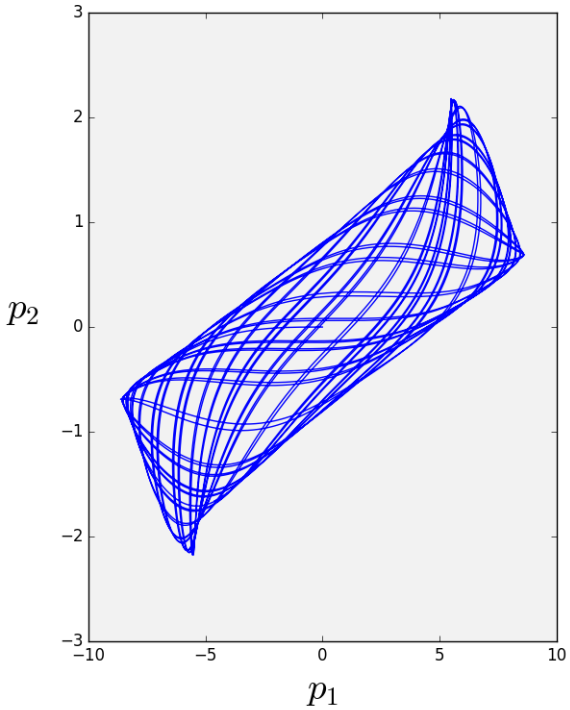

(d) p_1 vs p_2

Figure 5: Quasiperiodic Motion - Phase Space ($\boldsymbol{y}_0 = (0.8, 0, 0, 0)$, $T = 240$ seconds)

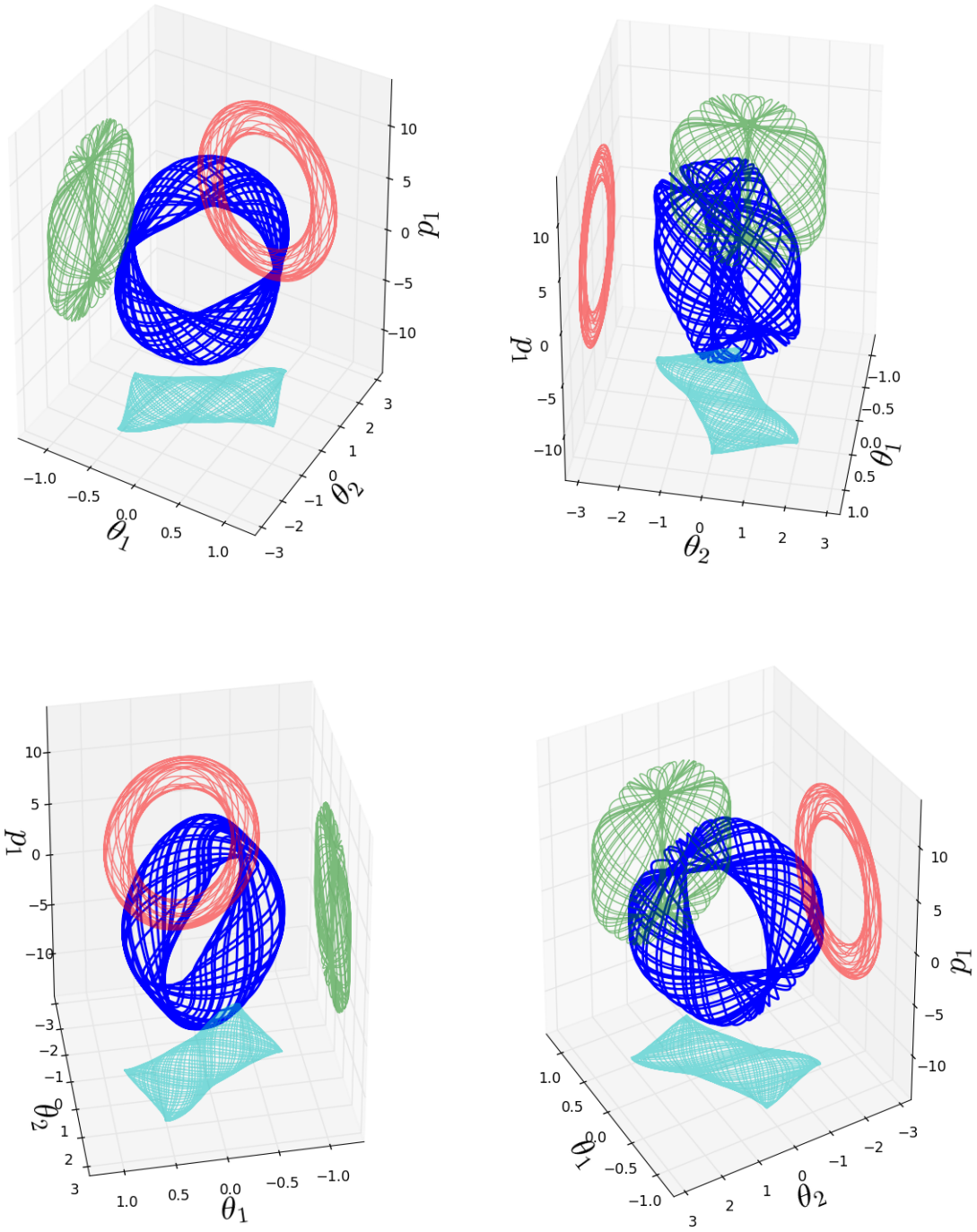

Figure 6: Quasiperiodic Motion - $(\theta_1, \theta_2, p_1)$ Phase Space ($\boldsymbol{y}_0 = (0.8, 0, 0, 0)$, $T = 240$ seconds)

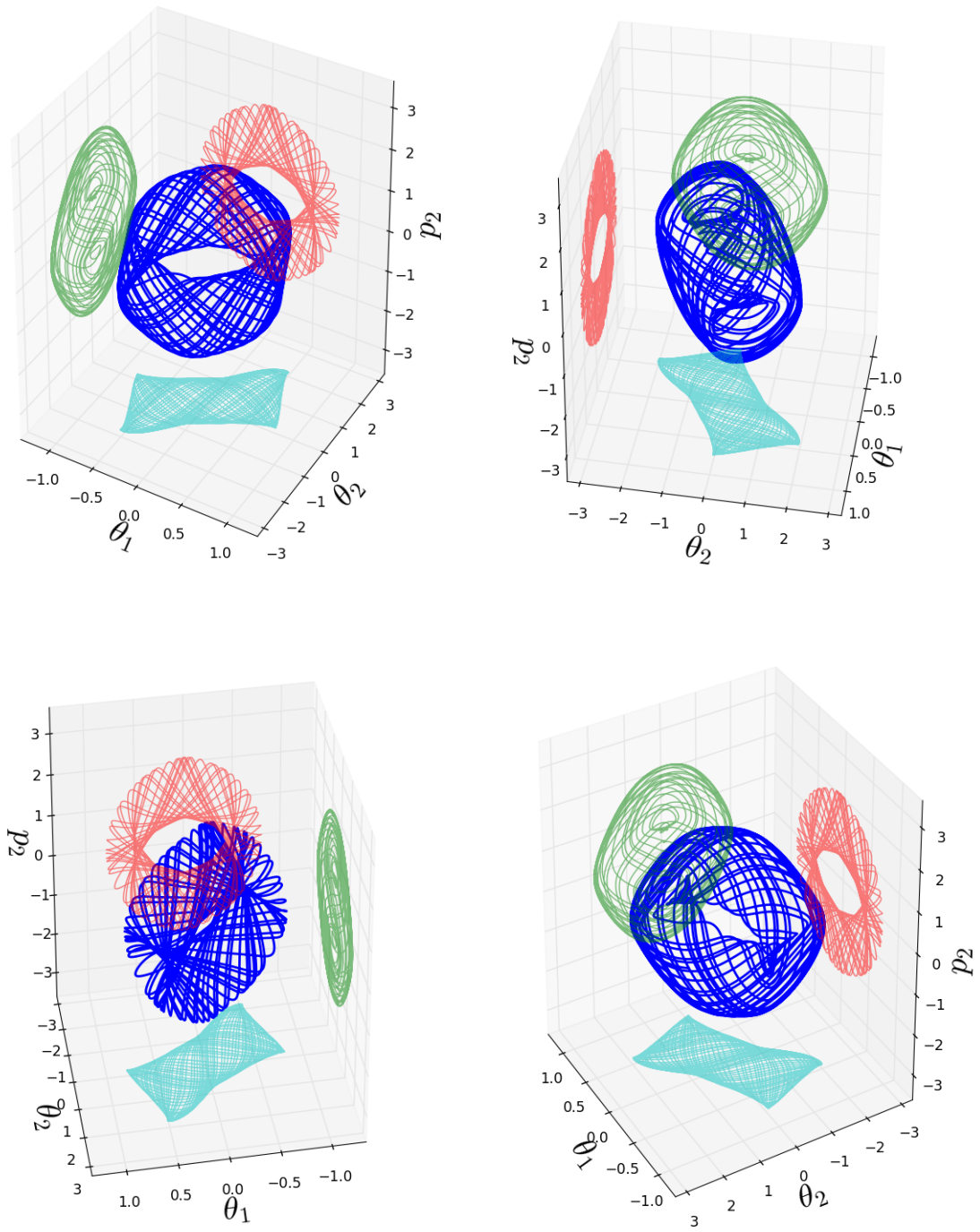

Figure 7: Quasiperiodic Motion - $(\theta_1, \theta_2, p_2)$ Phase Space ($\boldsymbol{y}_0 = (0.8, 0, 0, 0)$, $T = 240$ seconds)

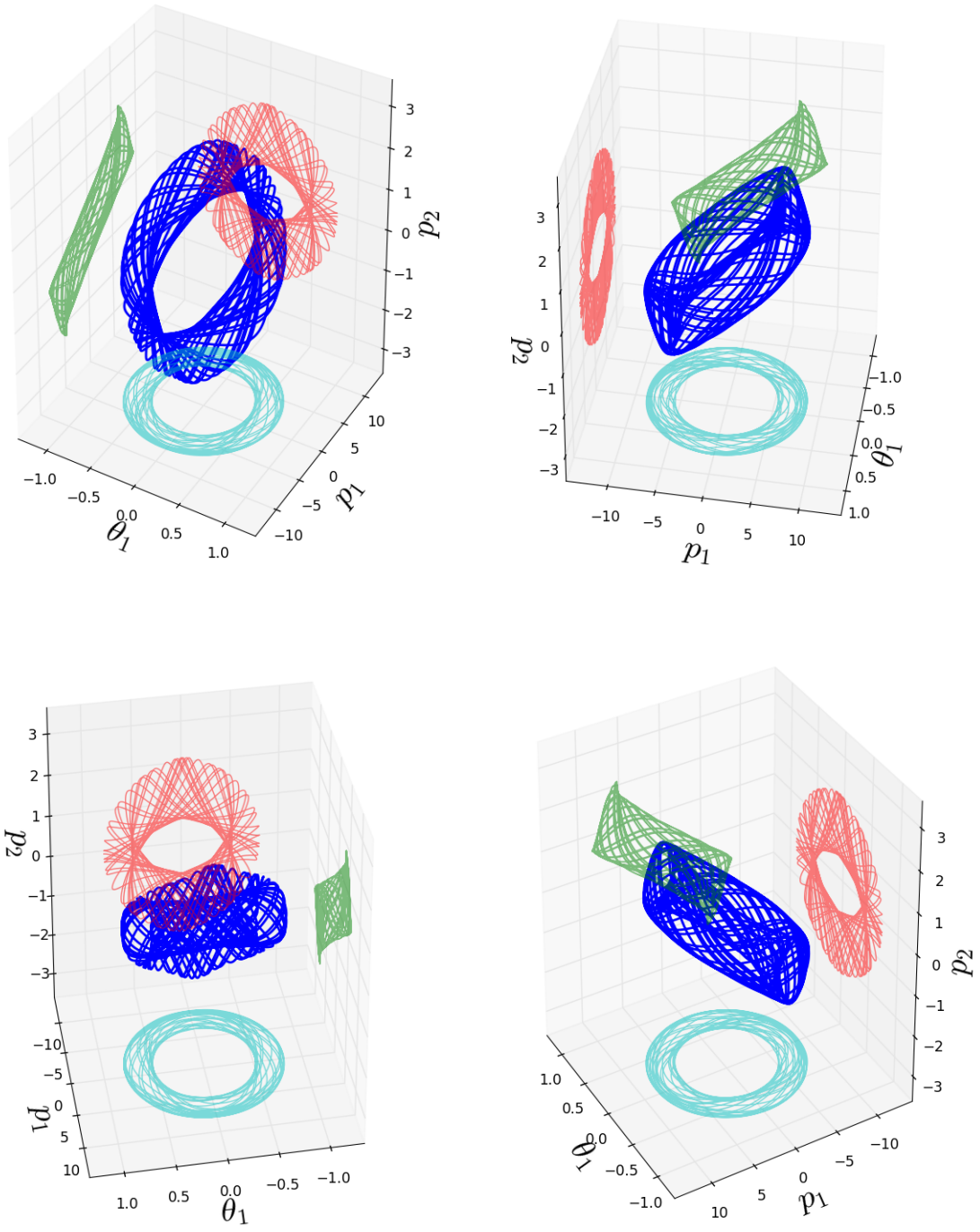

Figure 8: Quasiperiodic Motion - (θ_1, p_1, p_2) Phase Space ($\boldsymbol{y}_0 = (0.8, 0, 0, 0)$, $T = 240$ seconds)

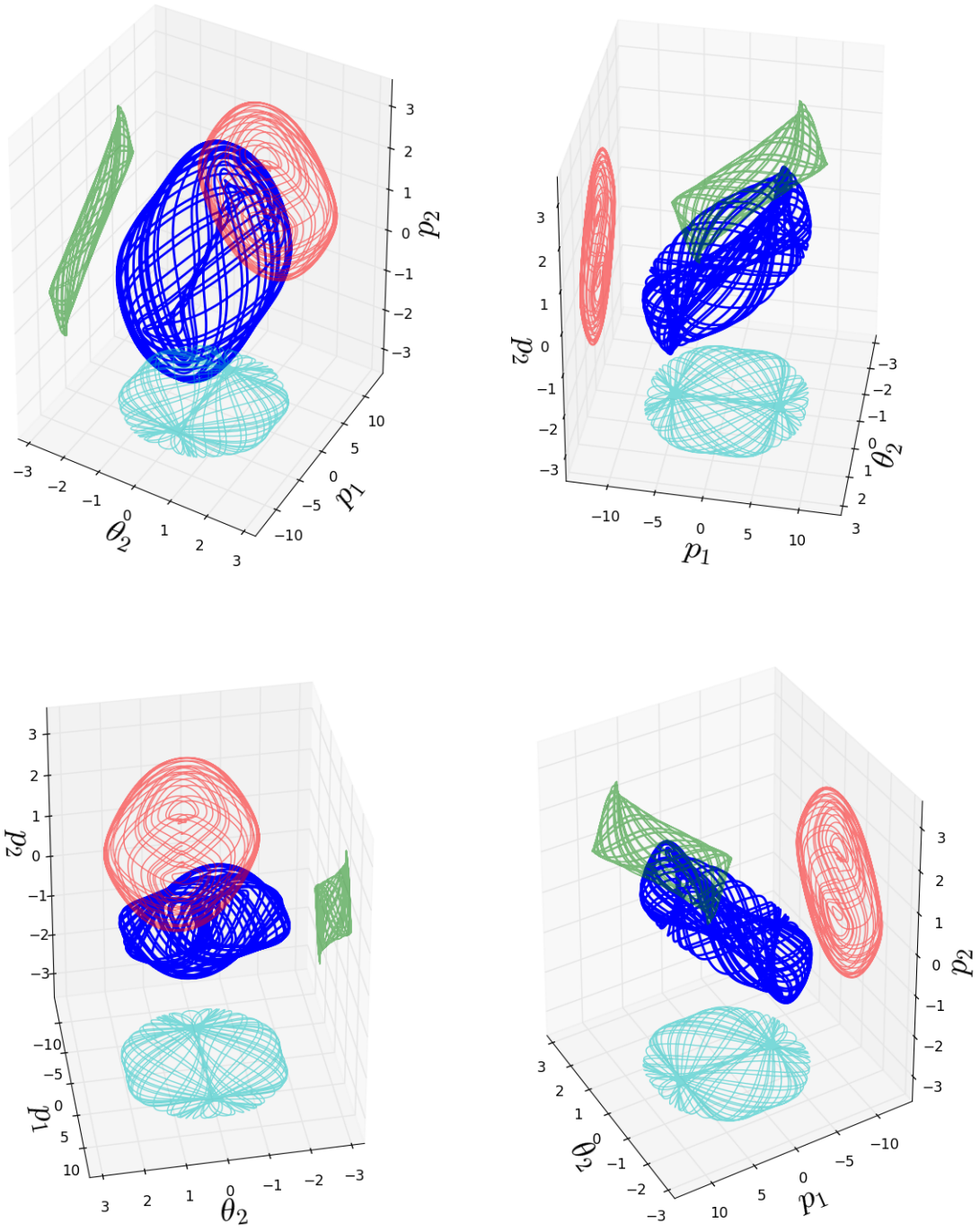

Figure 9: Quasiperiodic Motion - (θ_2, p_1, p_2) Phase Space ($\boldsymbol{y}_0 = (0.8, 0, 0, 0)$, $T = 240$ seconds)

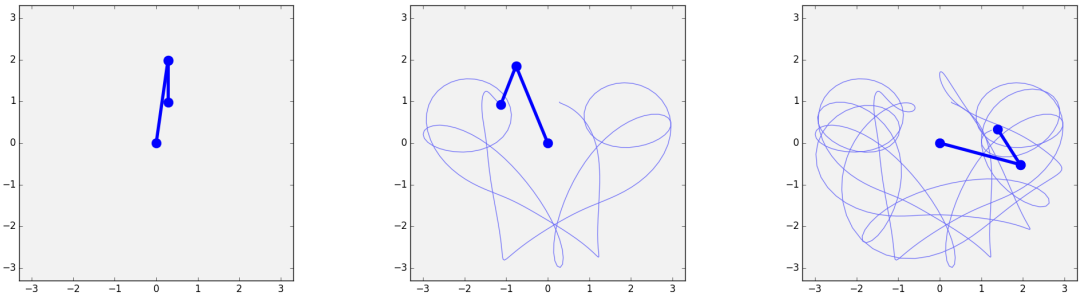

(a) $t = 0$ (b) $t = 21.77$ (c) $t = 43.61$

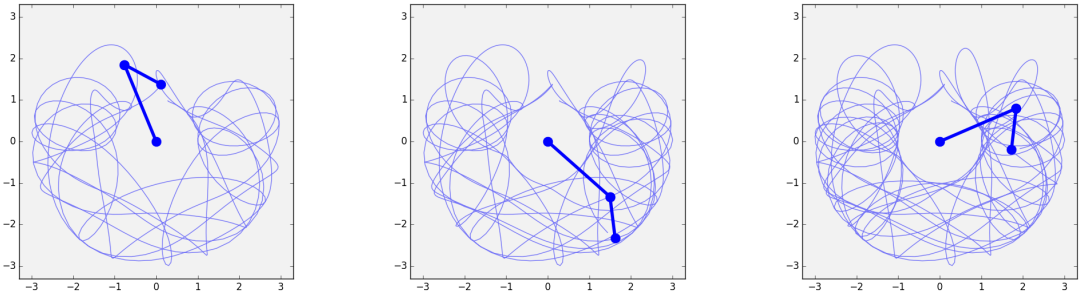

(d) $t = 65.45$ (e) $t = 87.22$ (f) $t = 109.06$

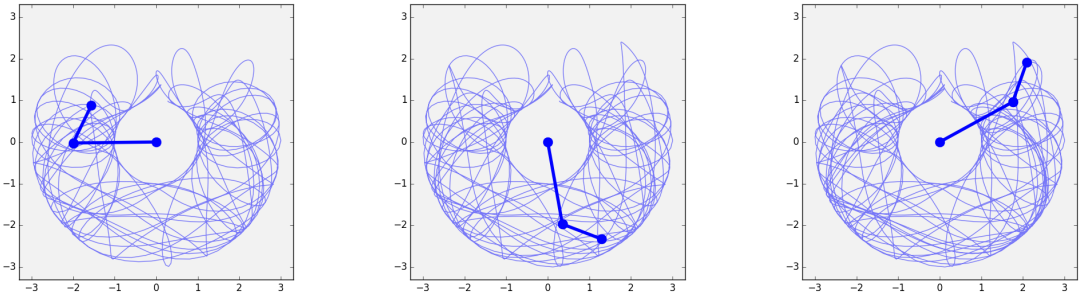

(g) $t = 130.9$ (h) $t = 152.74$ (i) $t = 174.51$

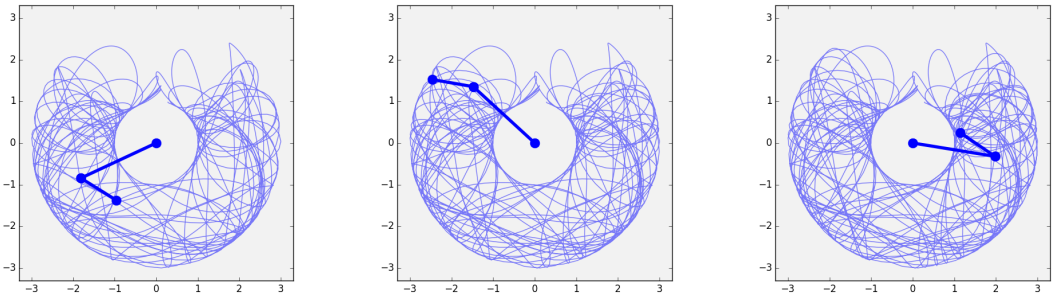

(j) $t = 196.35$ (k) $t = 218.19$ (l) $t = 240$

Figure 10: Chaotic Motion - Time Evolution

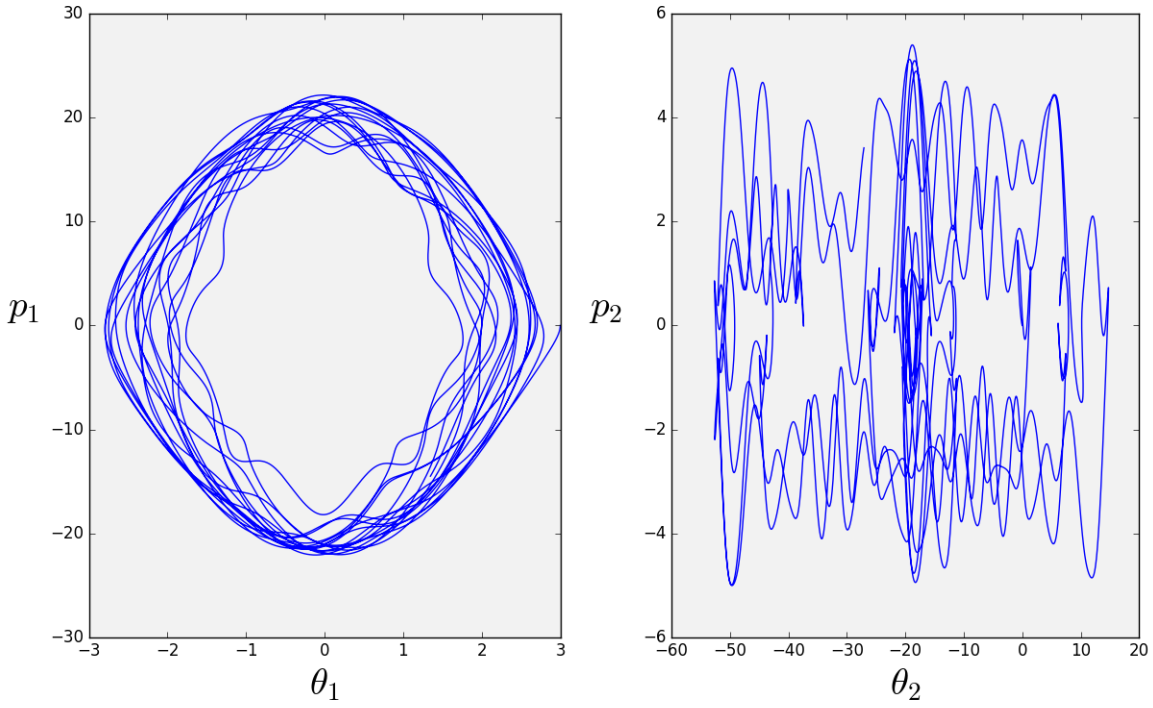

(a) θ_1 vs p_1

(b) θ_2 vs p_2

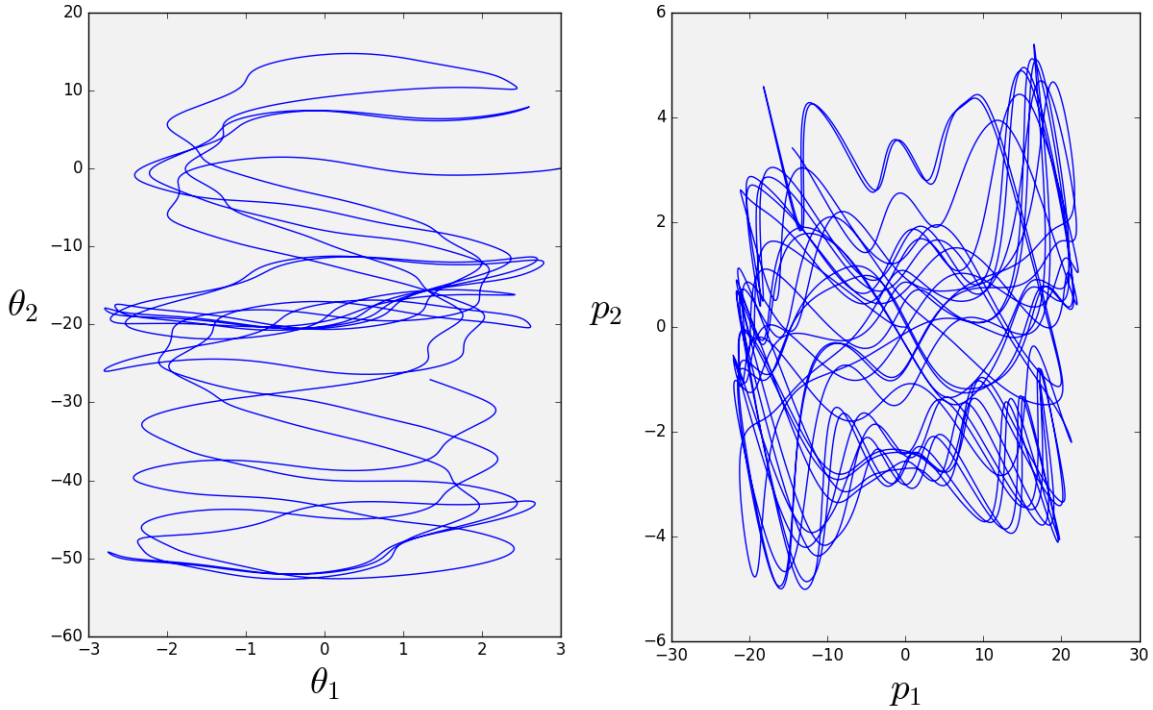

(c) θ_1 vs θ_2

(d) p_1 vs p_2

Figure 11: Chaotic Motion - Phase Space ($\boldsymbol{y}_0 = (3, 0, 0, 0)$, $T = 240$ seconds)

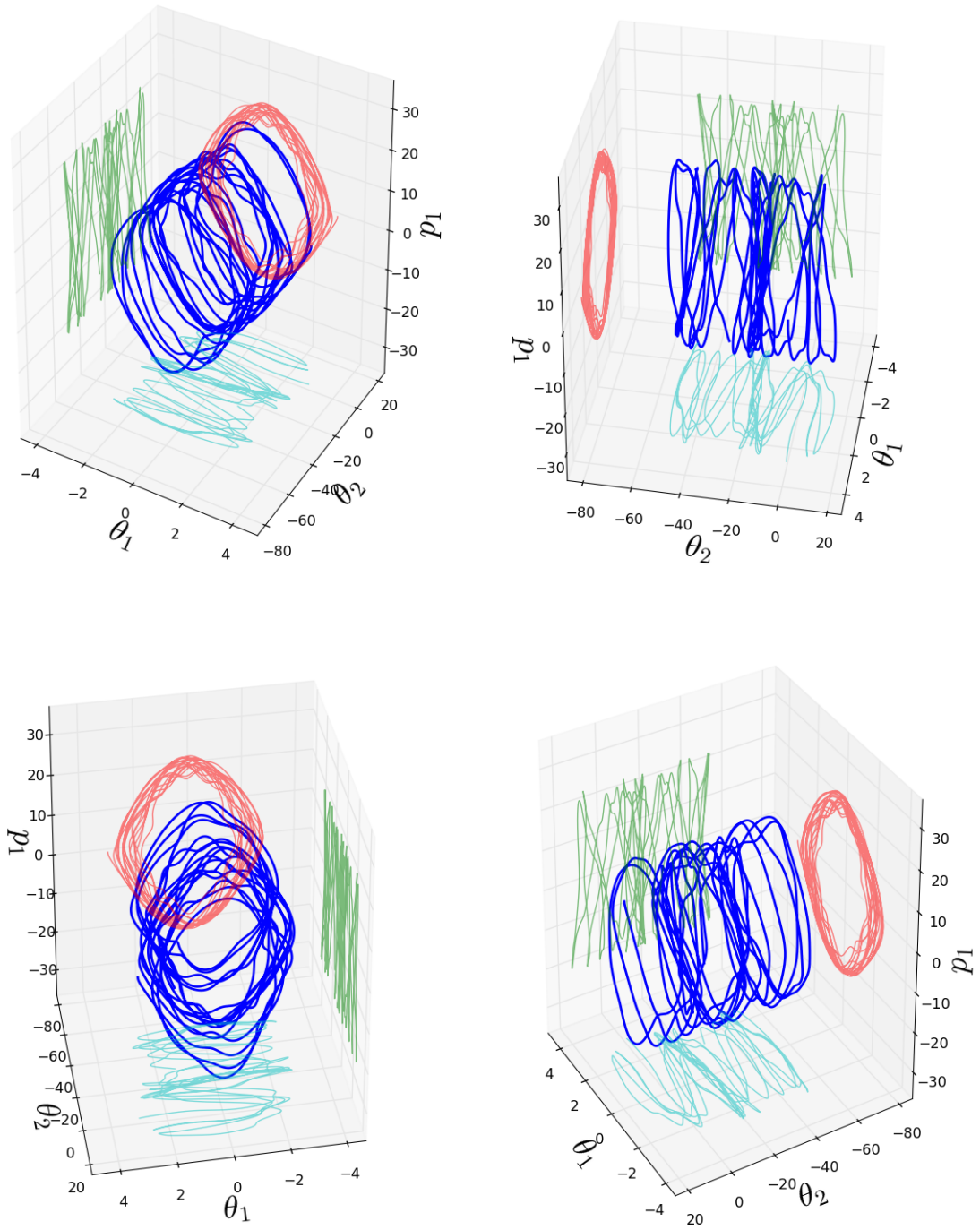

Figure 12: Chaotic Motion - $(\theta_1, \theta_2, p_1)$ Phase Space ($\boldsymbol{y}_0 = (3, 0, 0, 0)$, $T = 240$ seconds)

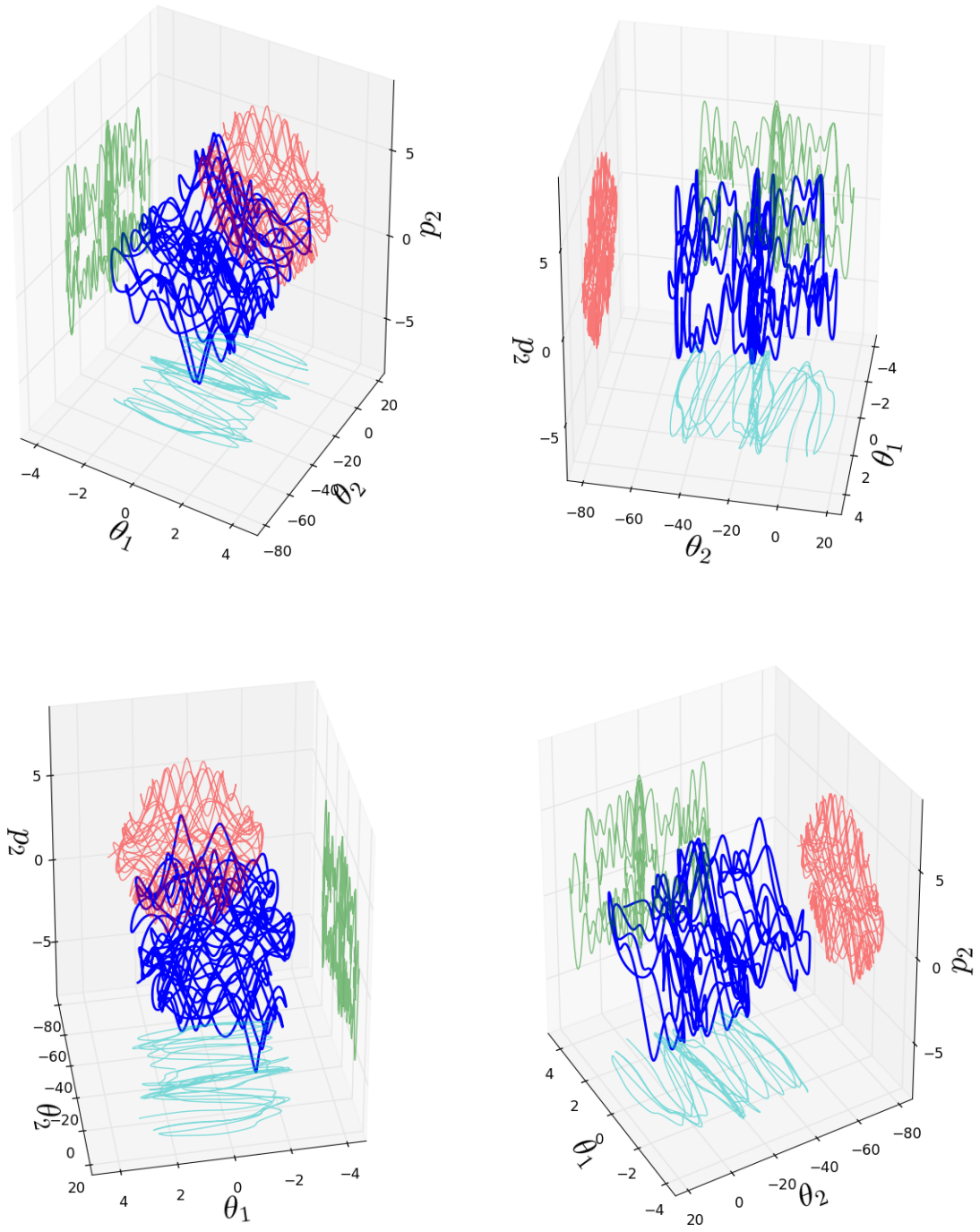

Figure 13: Chaotic Motion - $(\theta_1, \theta_2, p_2)$ Phase Space ($\boldsymbol{y}_0 = (3, 0, 0, 0)$, $T = 240$ seconds)

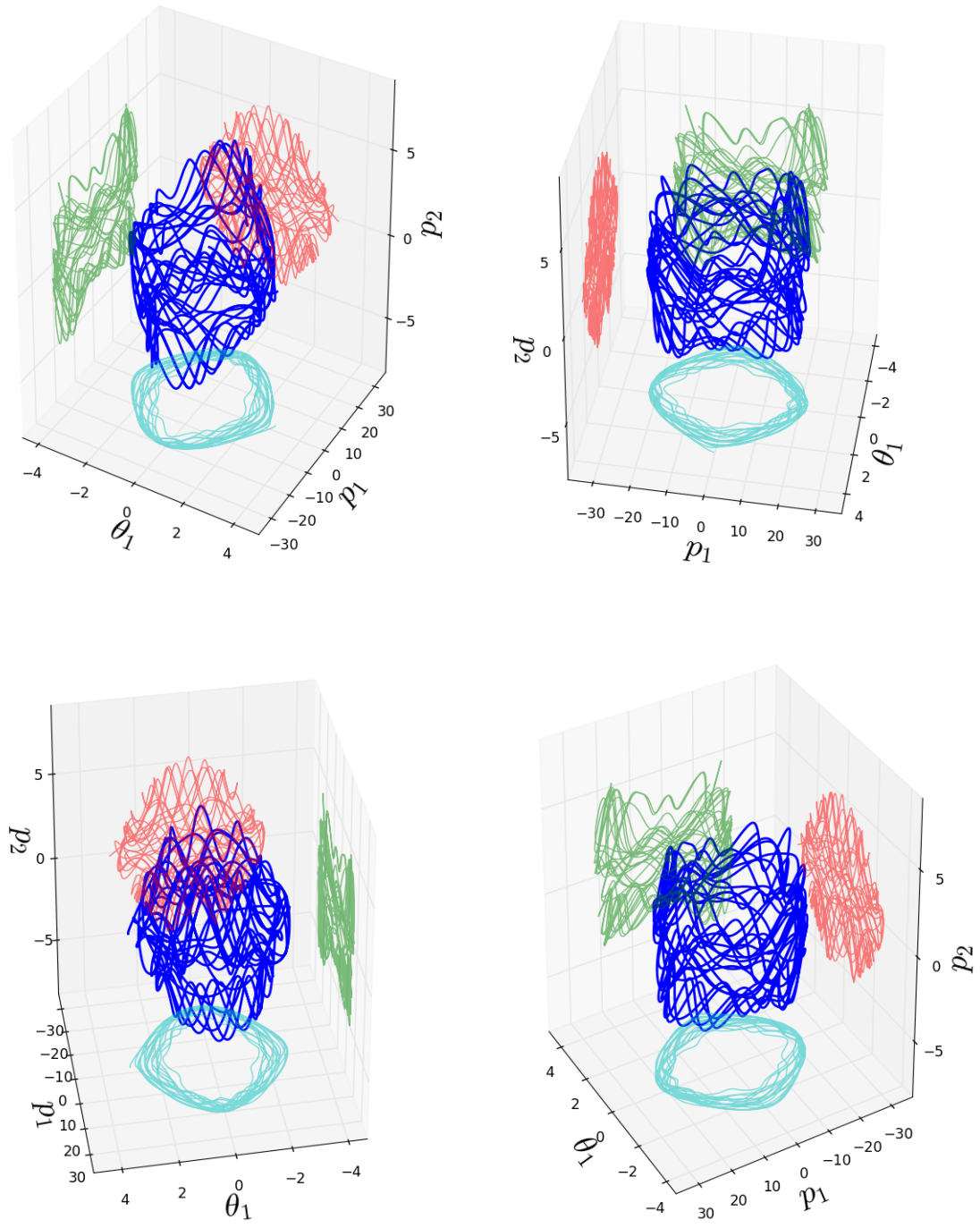

Figure 14: Chaotic Motion - (θ_1, p_1, p_2) Phase Space ($\boldsymbol{y}_0 = (3, 0, 0, 0)$, $T = 240$ seconds)

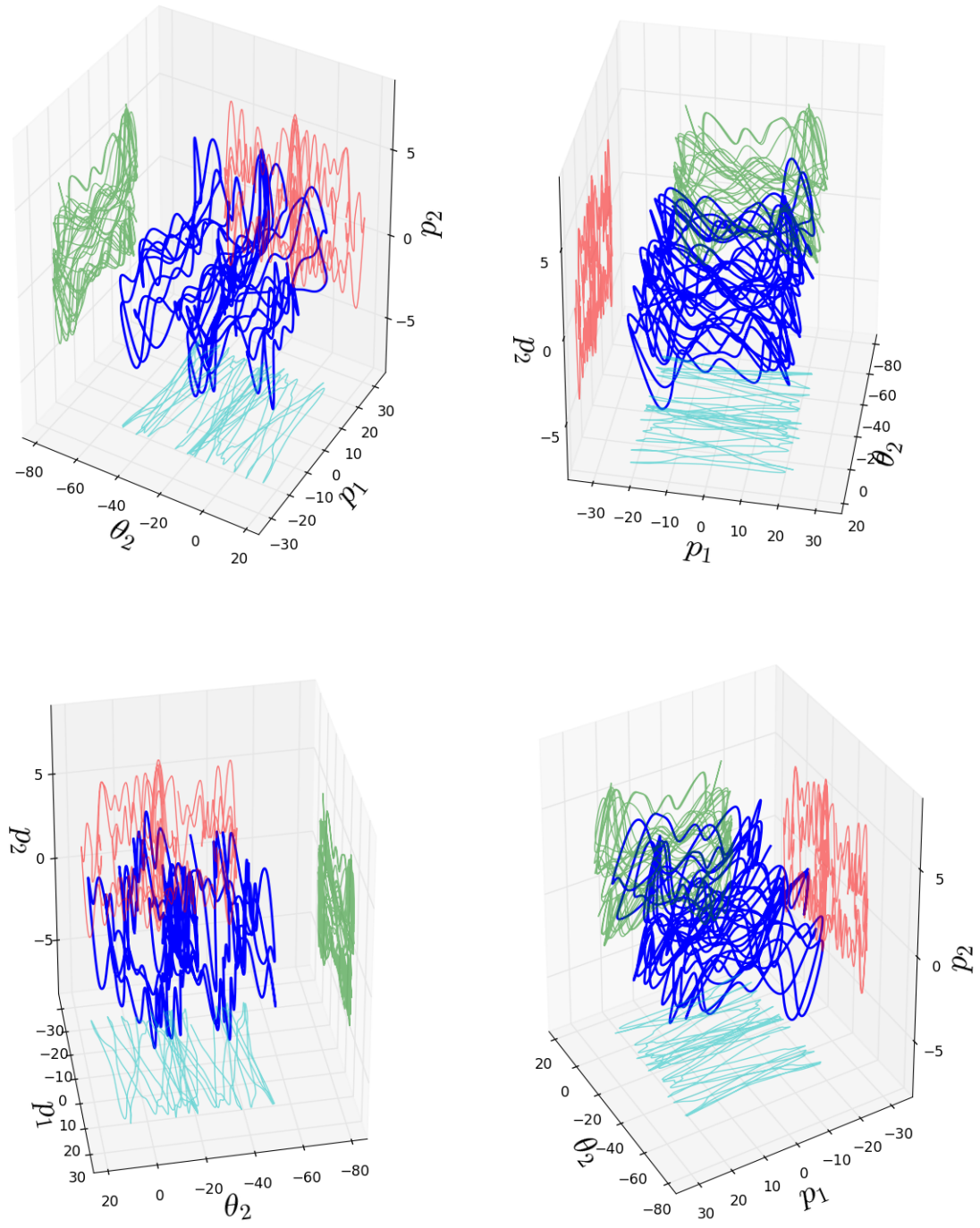

Figure 15: Chaotic Motion - (θ_2, p_1, p_2) Phase Space ($\boldsymbol{y}_0 = (3, 0, 0, 0)$, $T = 240$ seconds)

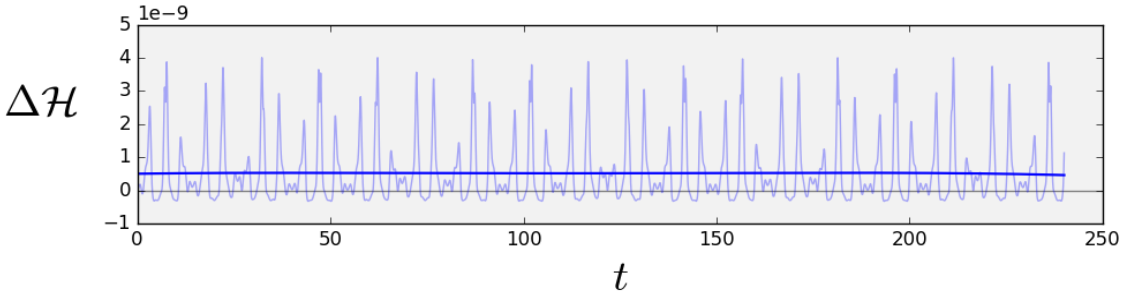

(a) Yoshida

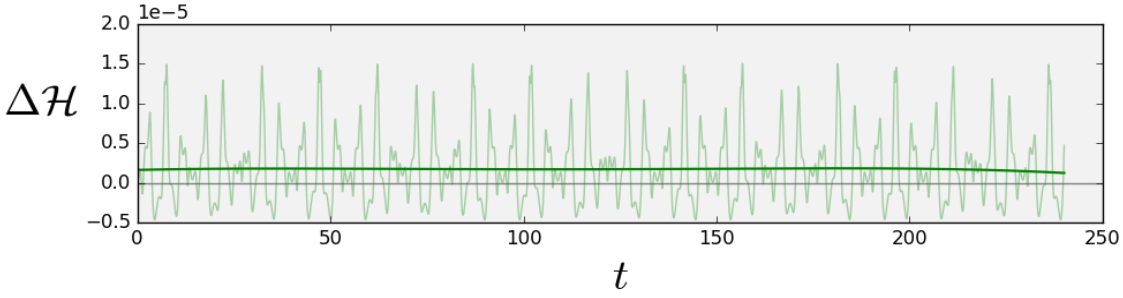

(b) Implicit Midpoint

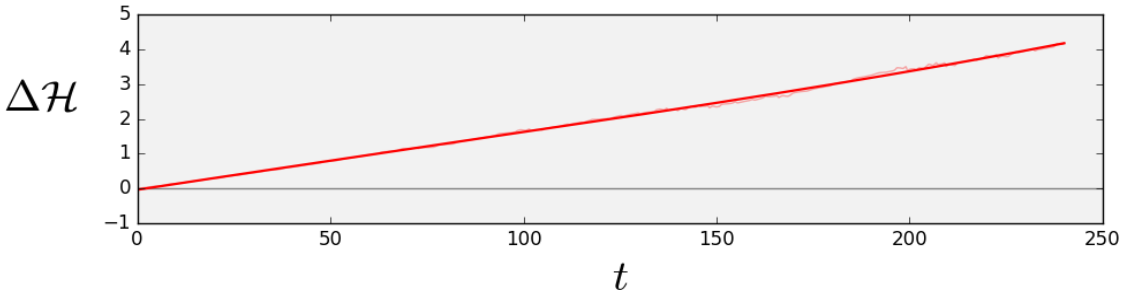

(c) Forward Euler

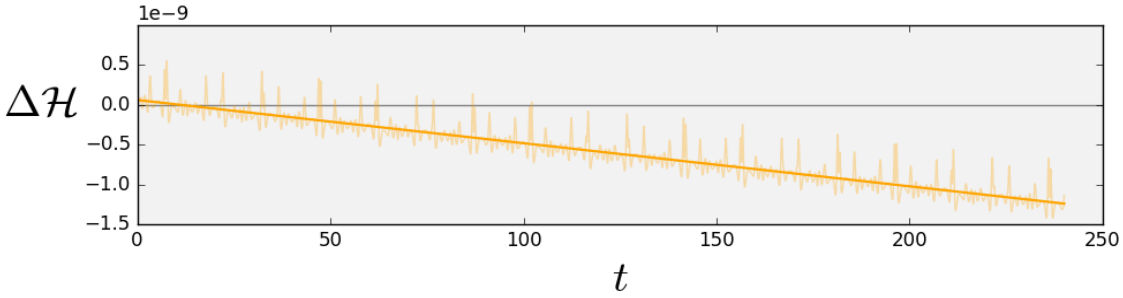

(d) Classic Runge-Kutta

Figure 16: Quasiperiodic Motion - Energy error ($T = 240$ seconds)

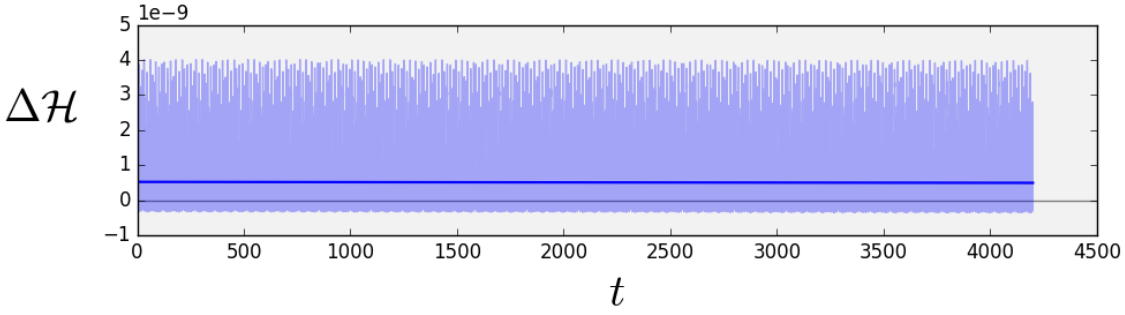

(a) Yoshida

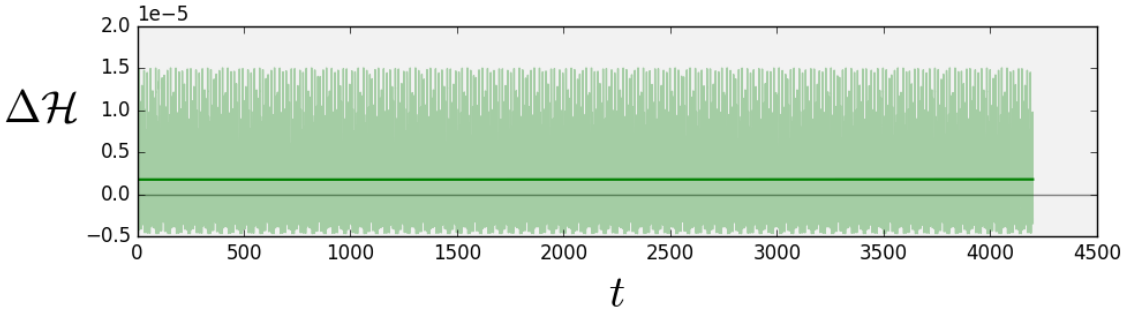

(b) Implicit Midpoint

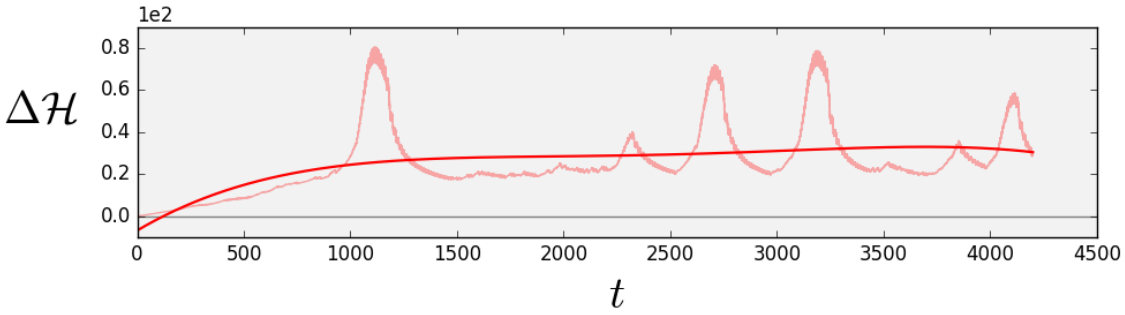

(c) Forward Euler

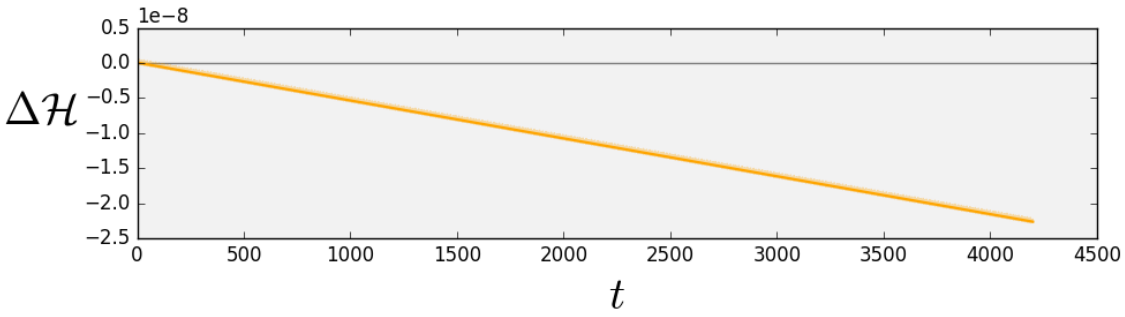

(d) Classic Runge-Kutta

Figure 17: Quasiperiodic Motion - Energy error ($T = 4200$ seconds)

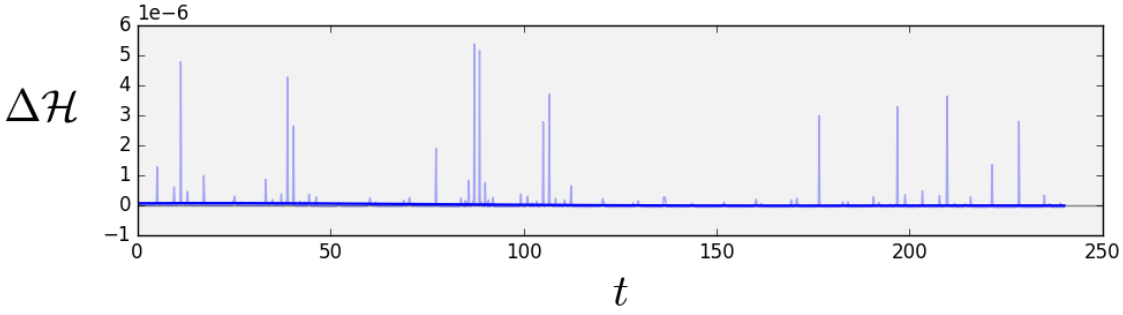

(a) Yoshida

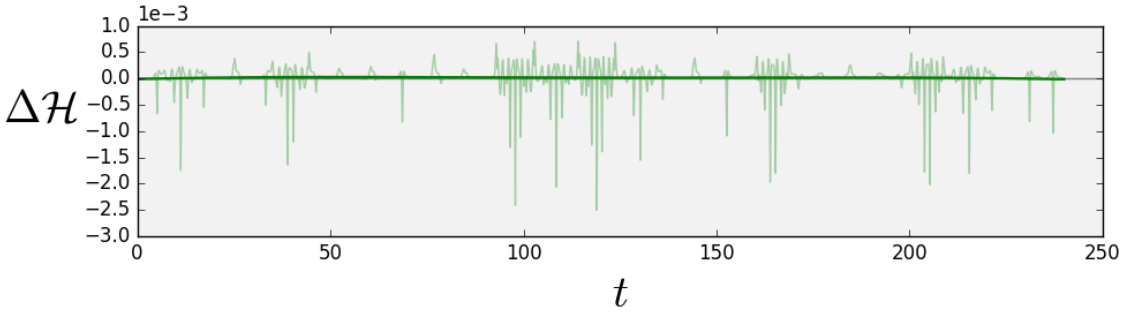

(b) Implicit Midpoint

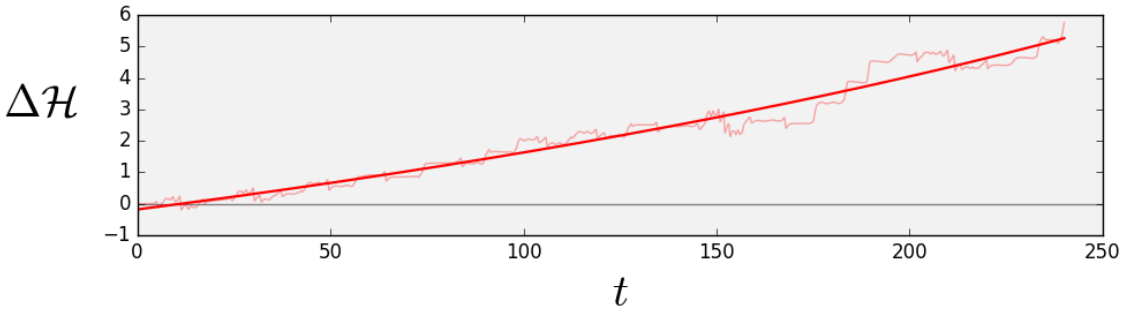

(c) Forward Euler

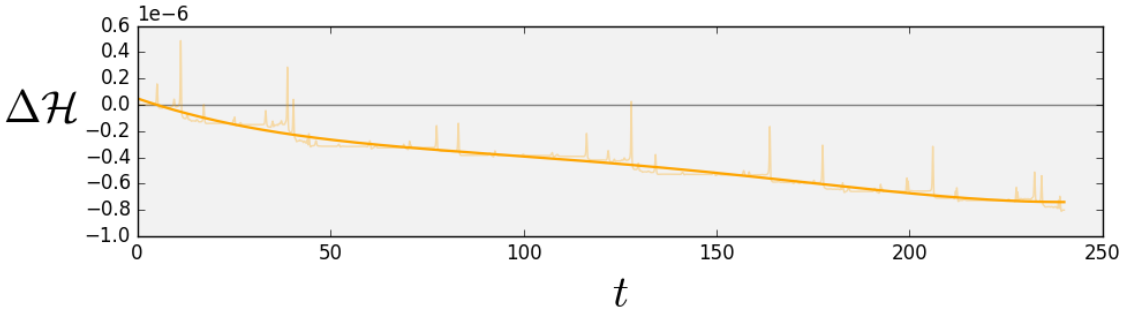

(d) Classic Runge-Kutta

Figure 18: Chaotic Motion - Energy error ($T = 240$ seconds)

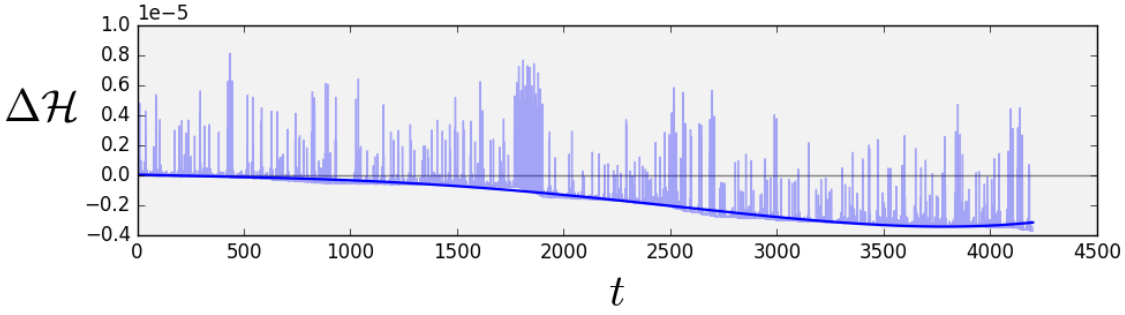

(a) Yoshida

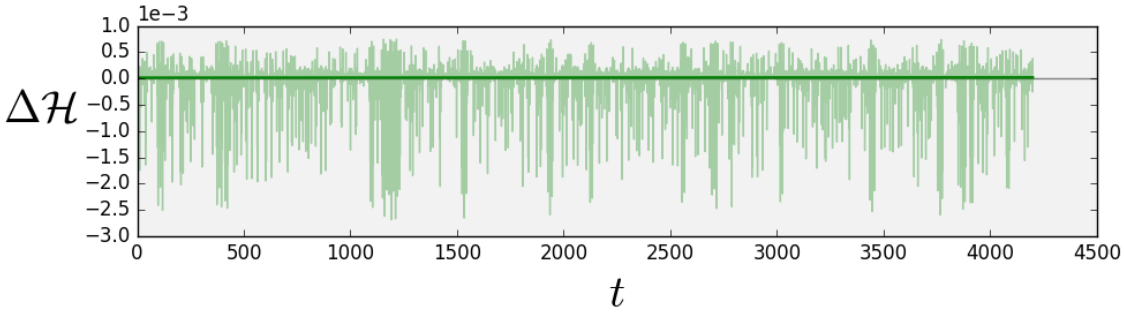

(b) Implicit Midpoint

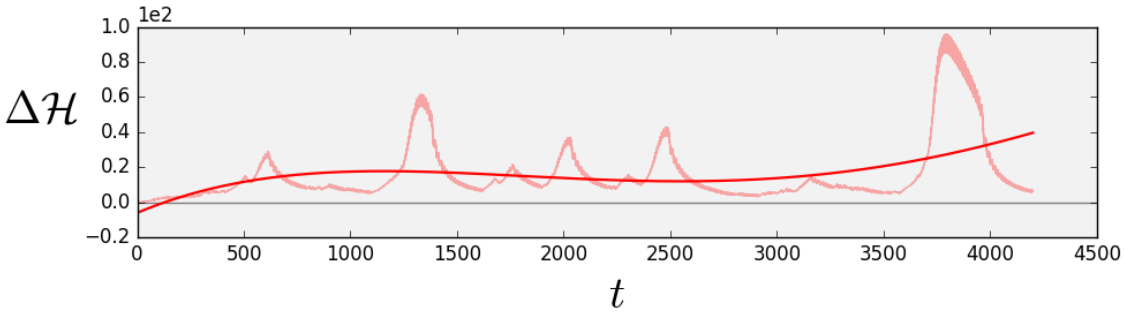

(c) Forward Euler

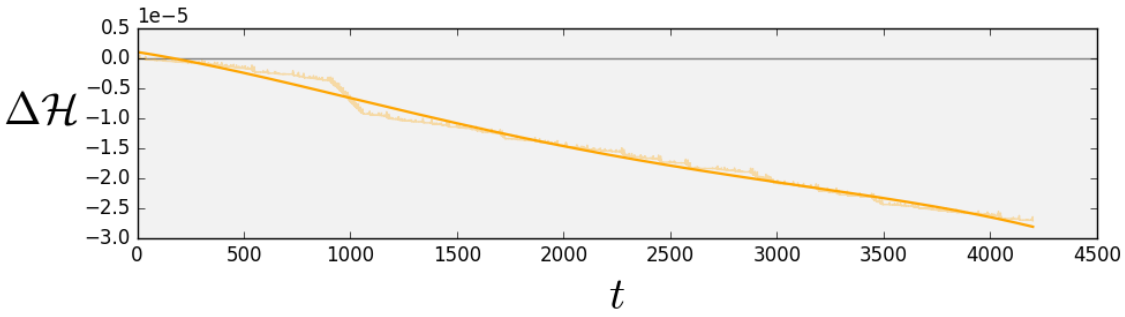

(d) Classic Runge-Kutta

Figure 19: Chaotic Motion - Energy error ($T = 4200$ seconds)

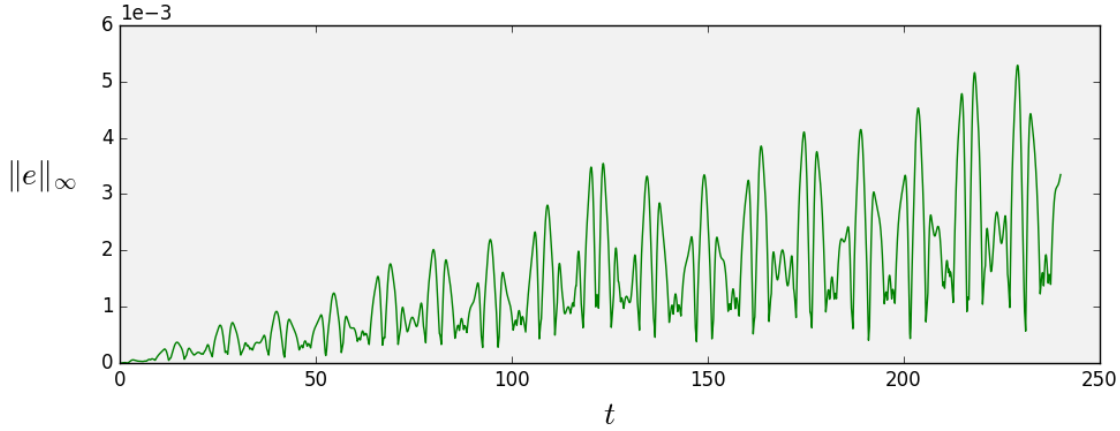

(a) Implicit Midpoint

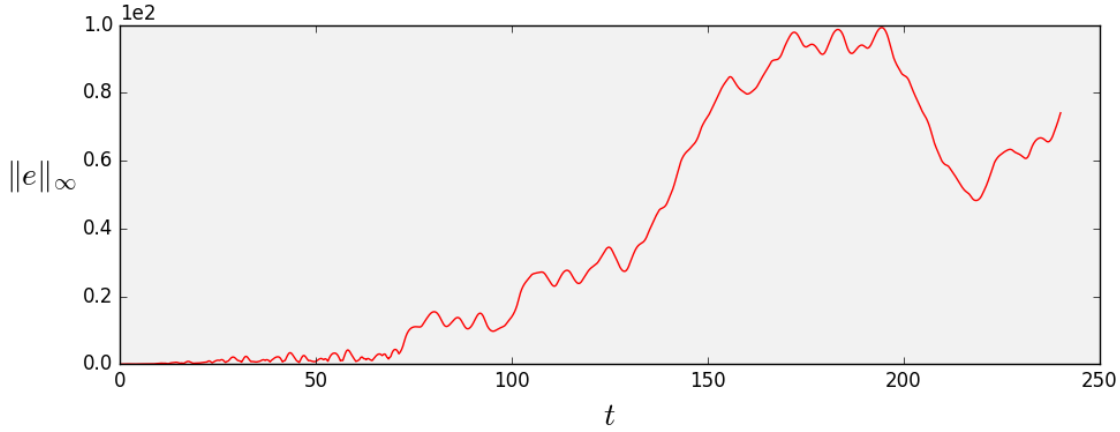

(b) Forward Euler

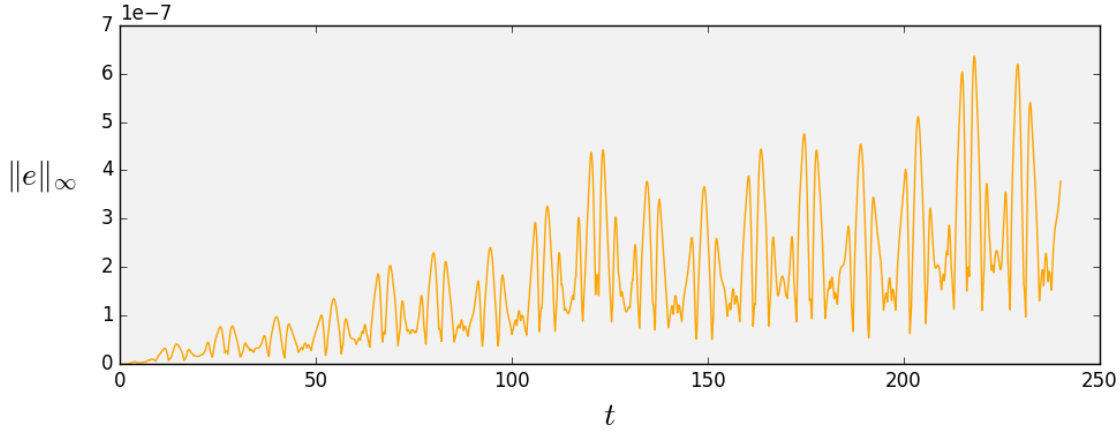

(c) Classic Runge-Kutta

Figure 20: Quasiperiodic Motion - Approximate error $\|\boldsymbol{e}\|_\infty$ ($T = 240$ seconds)

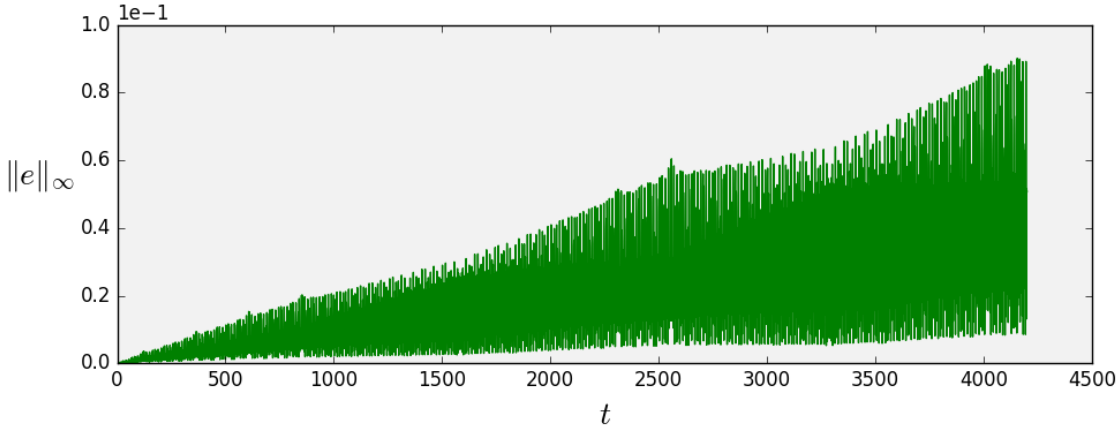

(a) Implicit Midpoint

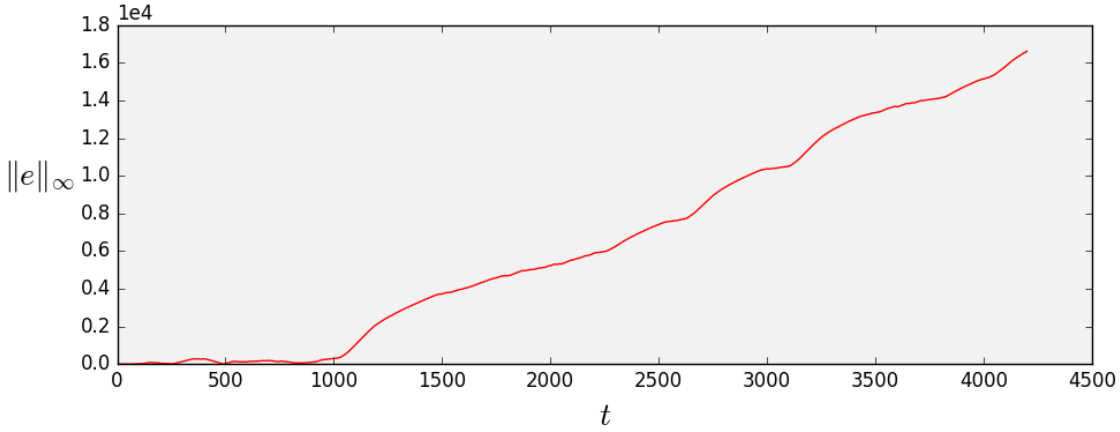

(b) Forward Euler

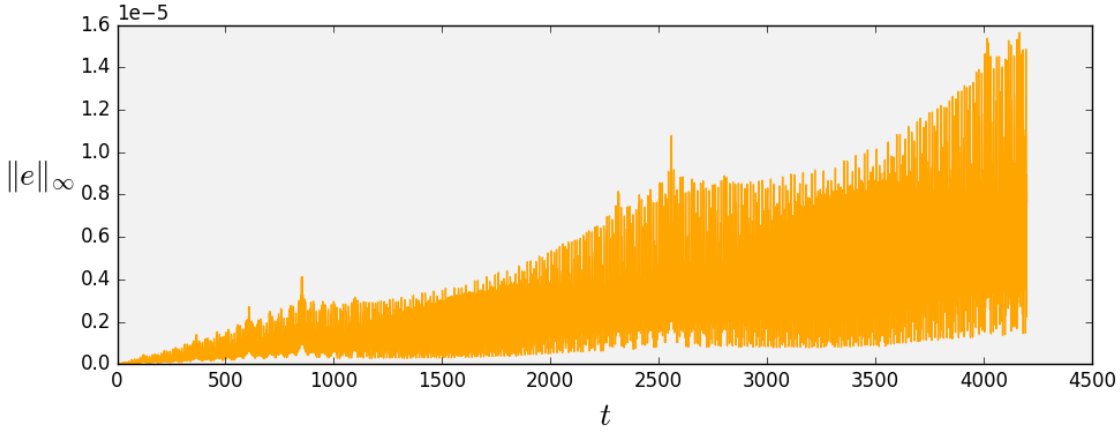

(c) Classic Runge-Kutta

Figure 21: Quasiperiodic Motion - Approximate error $\|\boldsymbol{e}\|_\infty$ ($T = 4200$ seconds)

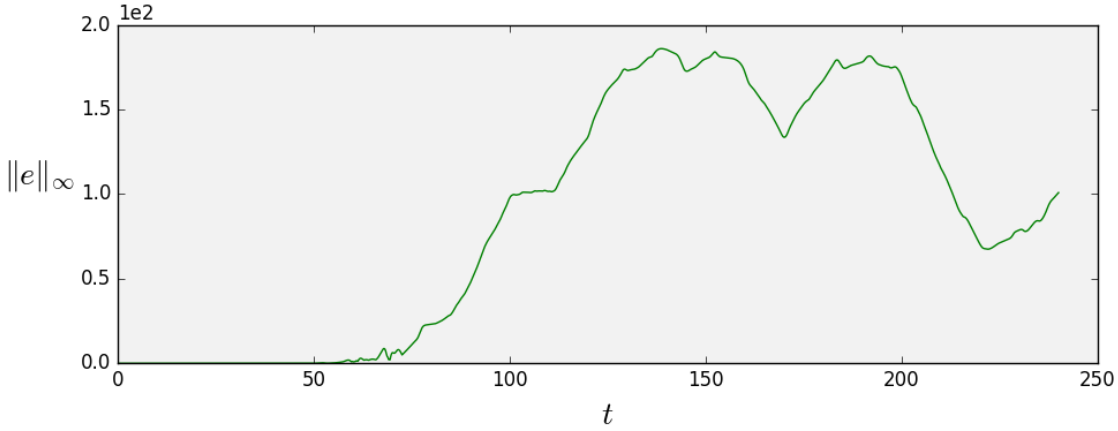

(a) Implicit Midpoint

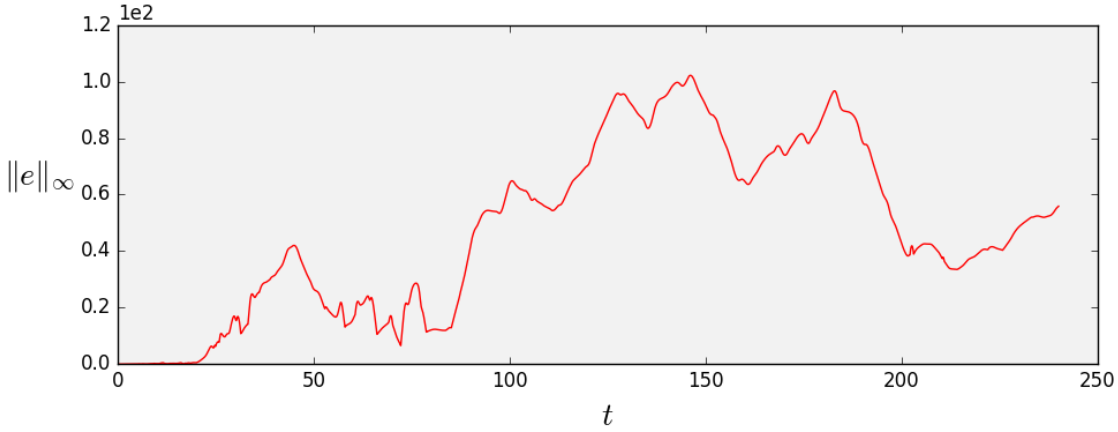

(b) Forward Euler

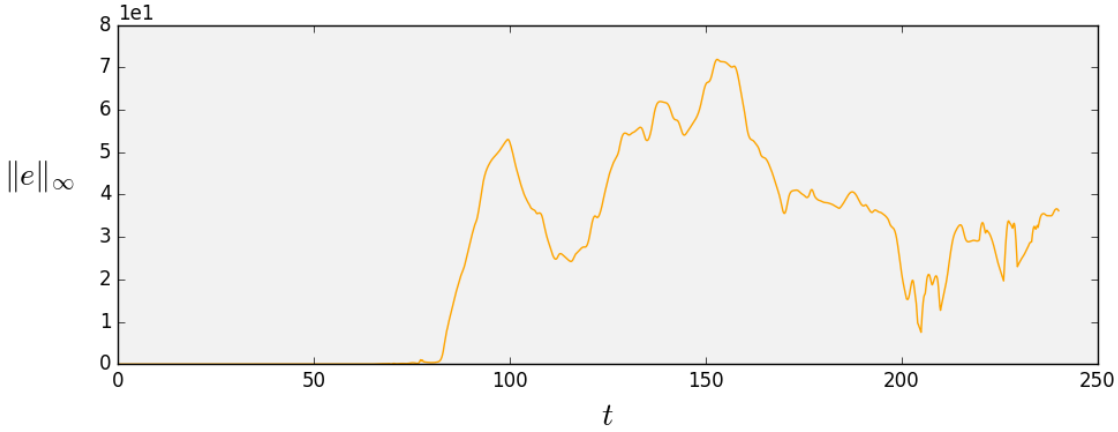

(c) Classic Runge-Kutta

Figure 22: Chaotic Motion - Approximate error $\|\boldsymbol{e}\|_\infty$ ($T = 240$ seconds)

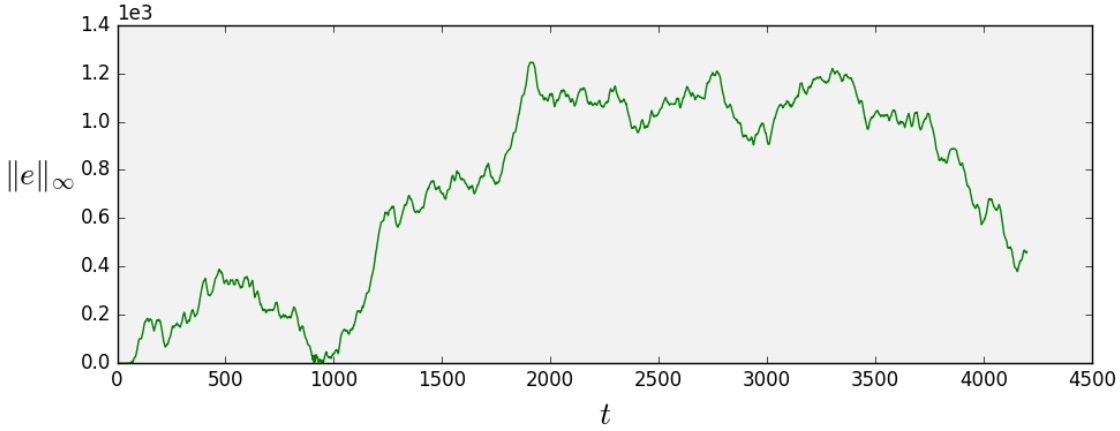

(a) Implicit Midpoint

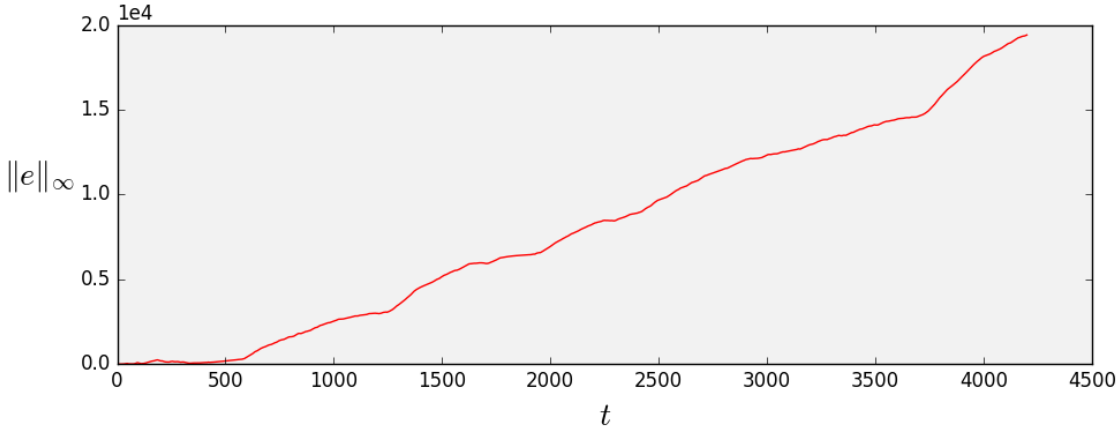

(b) Forward Euler

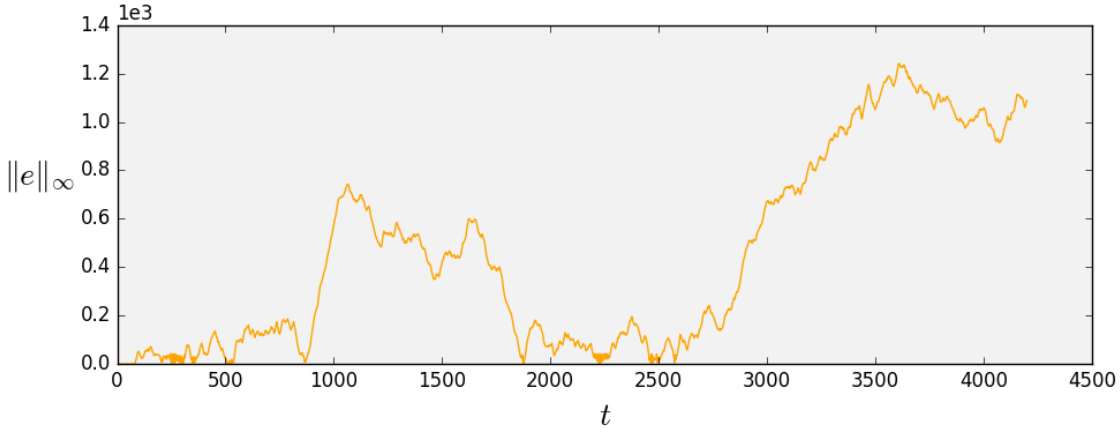

(c) Classic Runge-Kutta

Figure 23: Chaotic Motion - Approximate error $\|\boldsymbol{e}\|_\infty$ ($T = 4200$ seconds)

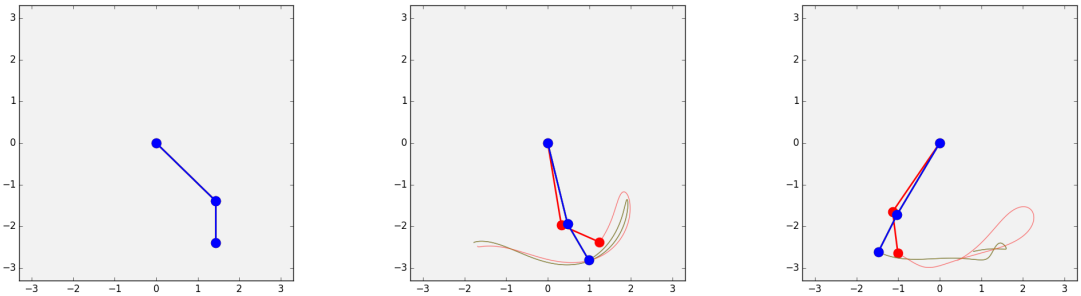

(a) $t = 0$ (b) $t = 21.7$ (c) $t = 43.6$

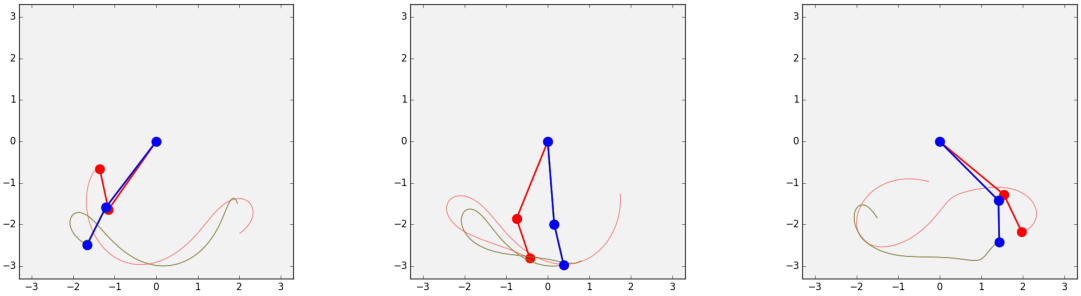

(d) $t = 65.42$ (e) $t = 87.24$ (f) $t = 109$

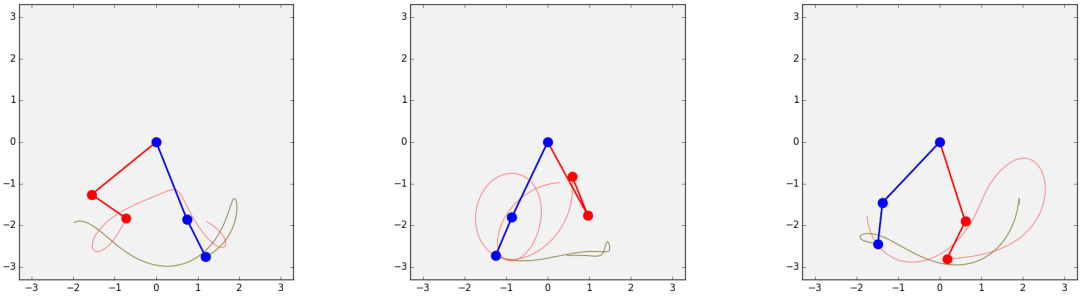

(g) $t = 130.87$ (h) $t = 152.69$ (i) $t = 174.51$

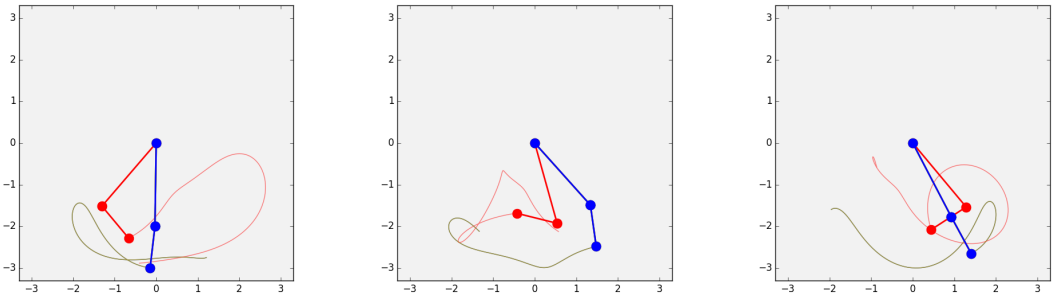

(j) $t = 196.33$ (k) $t = 218.16$ (l) $t = 240$

Figure 24: Quasiperiodic Motion - Comparison of numerical methods ($T = 240$ seconds) (Yoshida, Implicit Midpoint, Forward Euler, Classic Runge-Kutta)

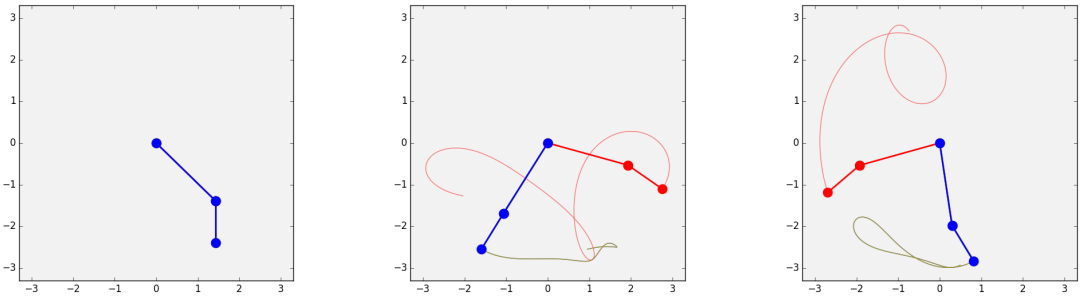

(a) $t = 0$ (b) $t = 381.7$ (c) $t = 763.6$

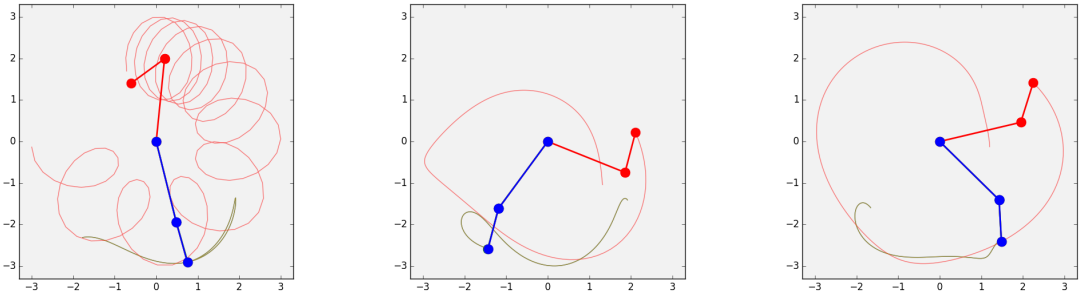

(d) $t = 1145.42$ (e) $t = 1527.24$ (f) $t = 1909$

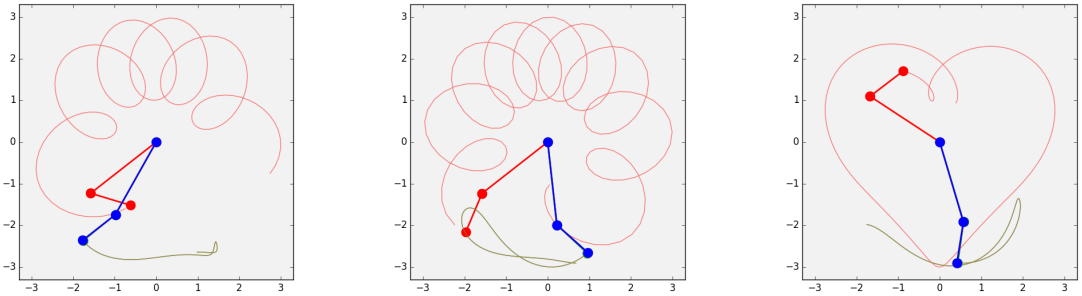

(g) $t = 2290.87$ (h) $t = 2672.69$ (i) $t = 3054.51$

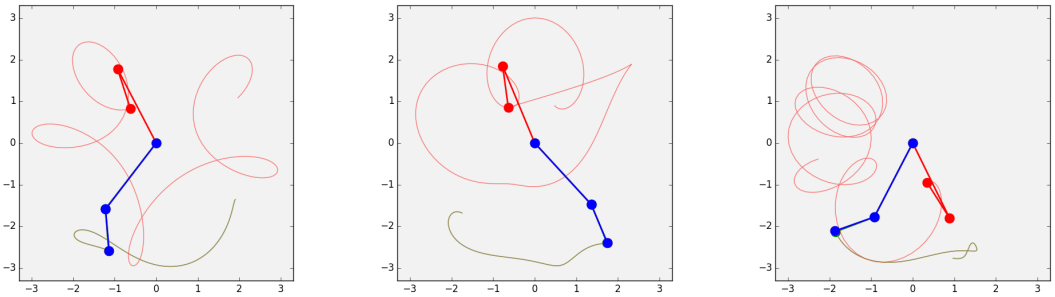

(j) $t = 3436.34$ (k) $t = 3818.16$ (l) $t = 4200$

Figure 25: Quasiperiodic Motion - Comparison of numerical methods ($T = 4200$ seconds) (Yoshida, Implicit Midpoint, Forward Euler, Classic Runge-Kutta)

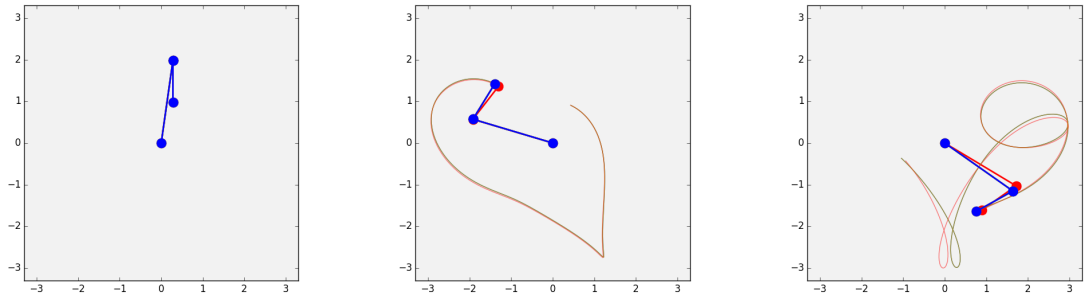

(a) $t = 0$ (b) $t = 8.15$ (c) $t = 16.33$

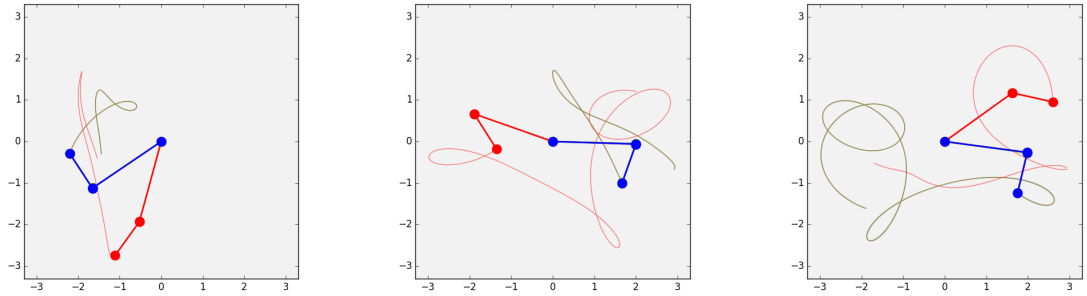

(d) $t = 24.51$ (e) $t = 32.69$ (f) $t = 40.87$

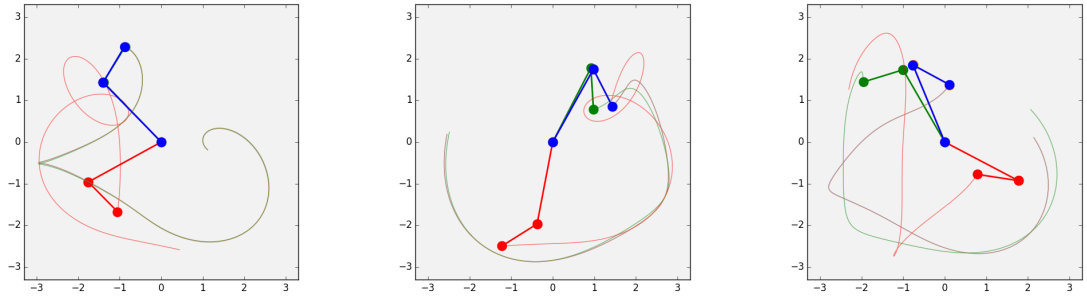

(g) $t = 49.06$ (h) $t = 57.24$ (i) $t = 65.42$

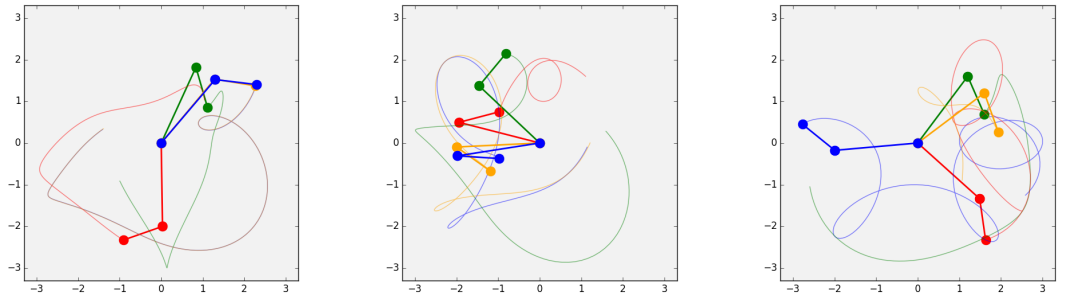

(j) $t = 73.60$ (k) $t = 81.78$ (l) $t = 90$

Figure 26: Chaotic Motion - Comparison of numerical methods ($T = 90$ seconds) (Yoshida, Implicit Midpoint, Forward Euler, Classic Runge-Kutta)

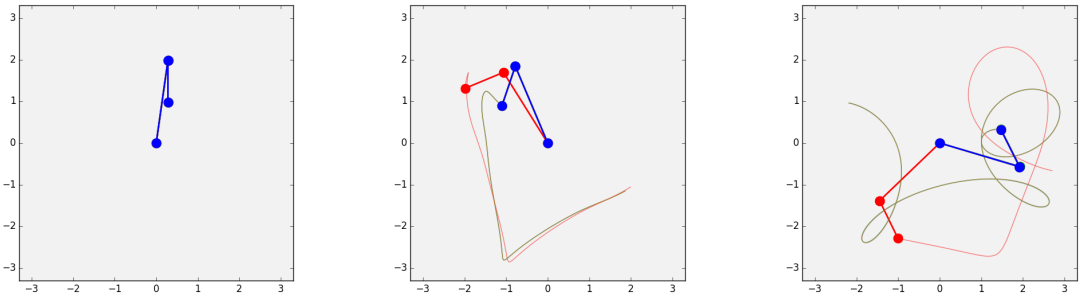

(a) $t = 0$ (b) $t = 21.7$ (c) $t = 43.6$

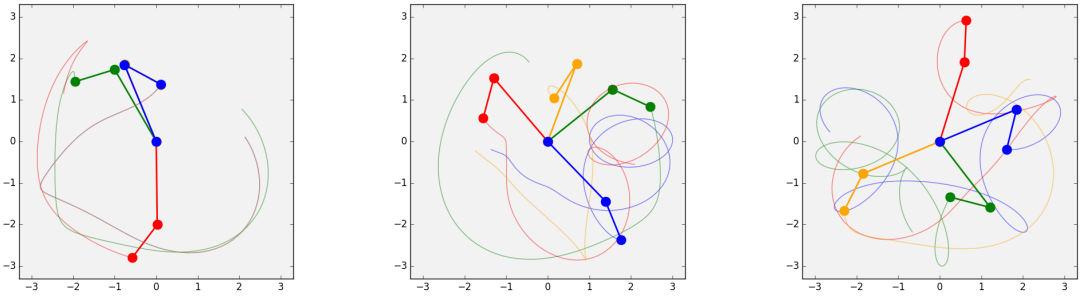

(d) $t = 65.42$ (e) $t = 87.24$ (f) $t = 109$

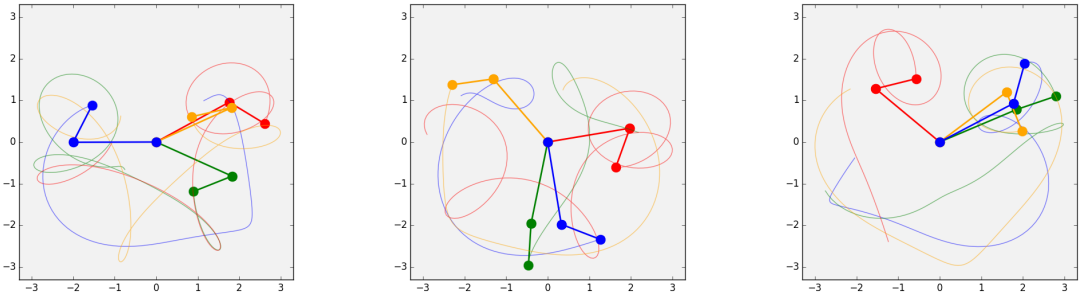

(g) $t = 130.87$ (h) $t = 152.69$ (i) $t = 174.51$

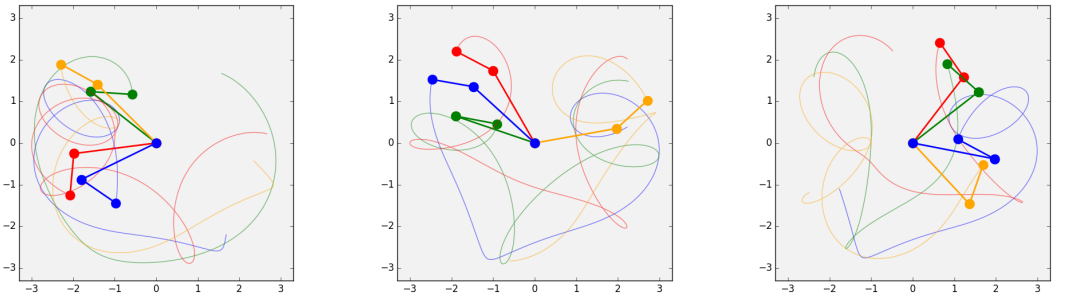

(j) $t = 196.33$ (k) $t = 218.16$ (l) $t = 240$

Figure 27: Chaotic Motion - Comparison of numerical methods ($T = 240$ seconds) (Yoshida, Implicit Midpoint, Forward Euler, Classic Runge-Kutta)

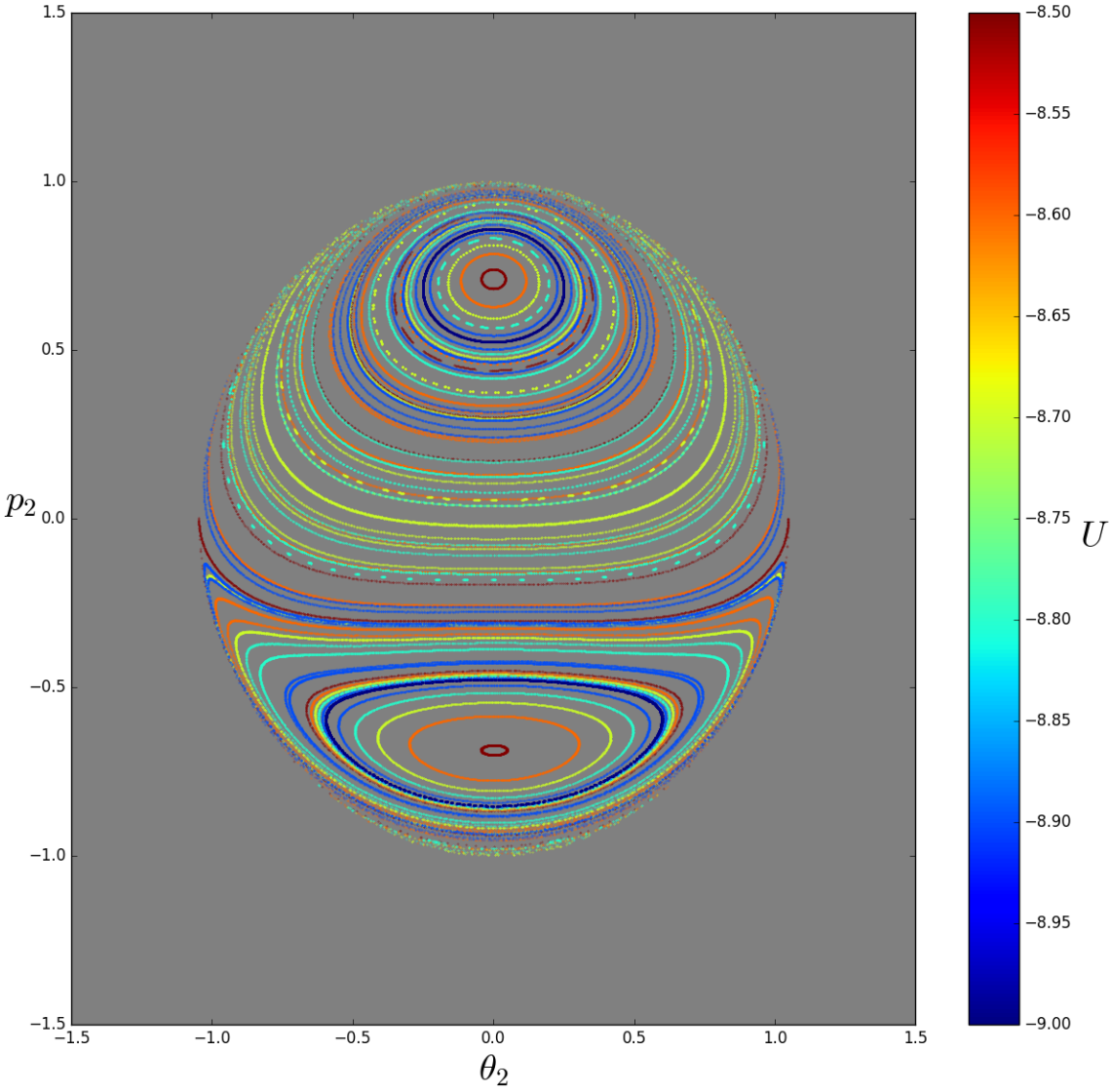

Figure 28: Poincare Map ($\mathcal{H}$= -8.5)

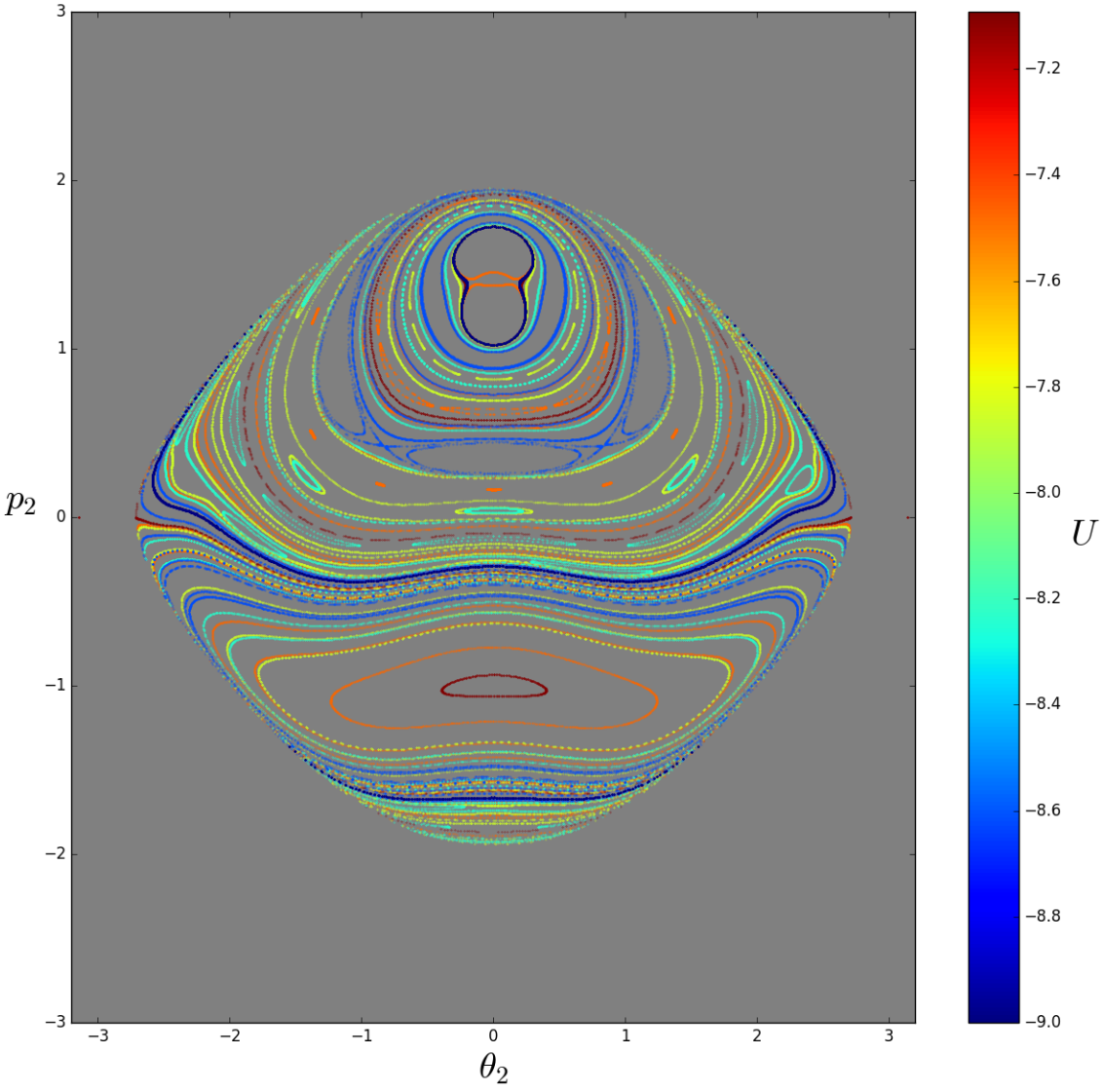

Figure 29: Poincare Map ($\mathcal{H}$= -7.1)

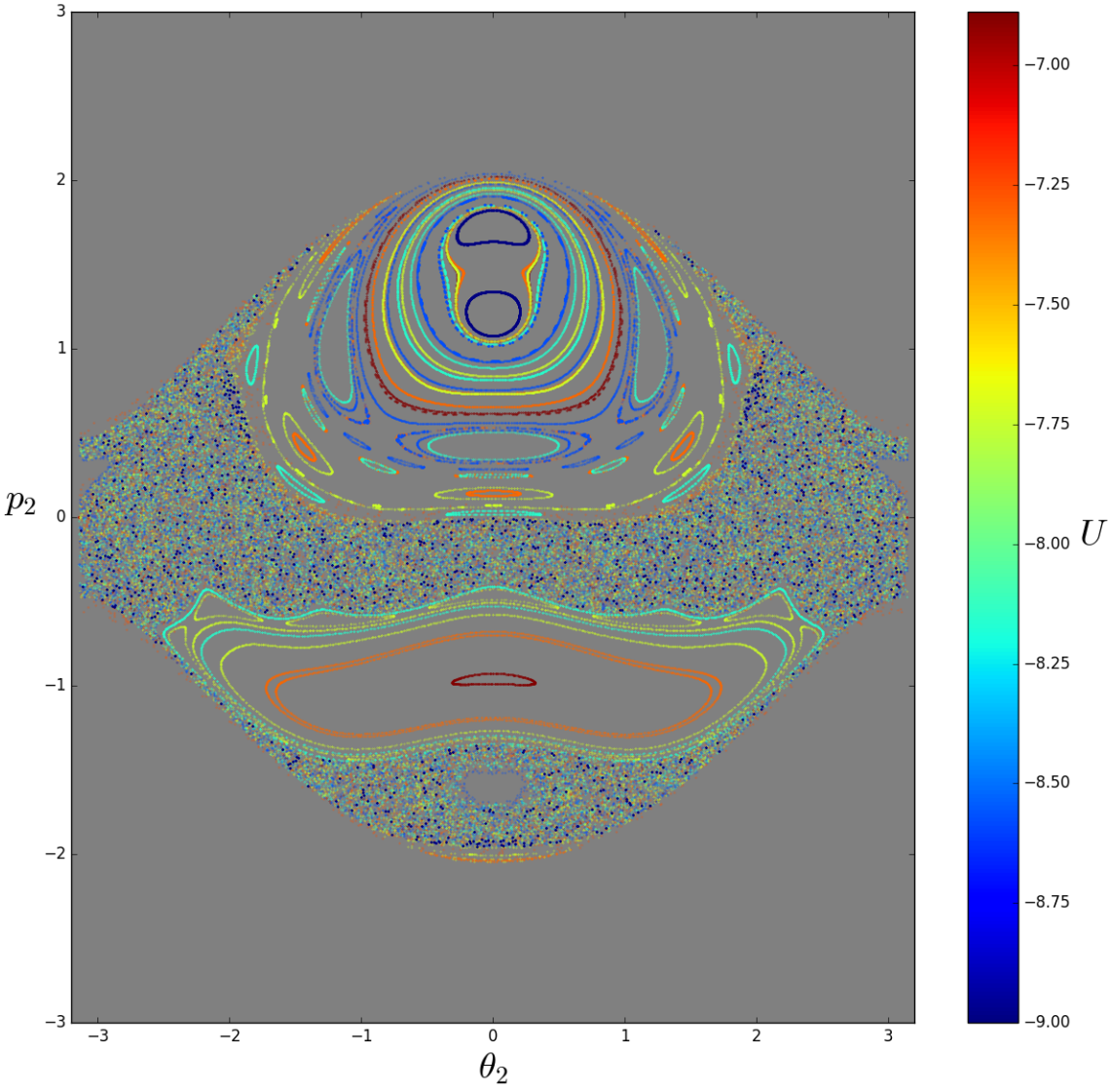

Figure 30: Poincare Map ($\mathcal{H}$= -6.9)

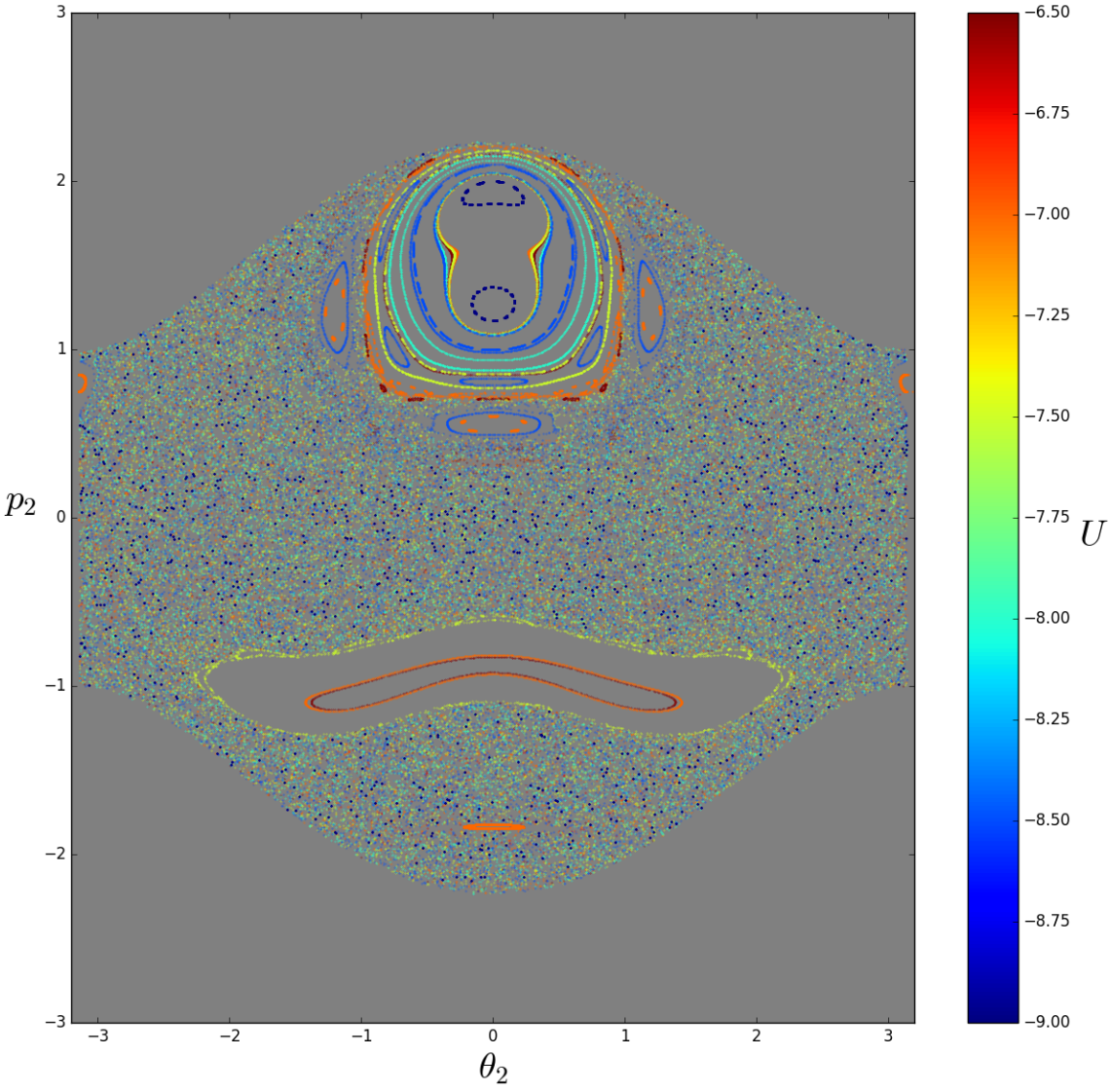

Figure 31: Poincare Map ($\mathcal{H}$= -6.5)

References

[1] Ernst Hairer. *Personal Collection of Ernst Hairer.* Technical University of Munich, Munich, German, 2010.

[2] Arieh Iserles. *A First Course in the Numerical Analysis of Differential Equations.* Cambridge University Press, Cambridge, United Kingdom, 2009.

[3] Edward Ott. *Chaos in Dynamical Systems.* Cambridge University Press, Cambridge, United Kingdom, 1993.

[4] Toshio Okada Tomasaz Stachowiak. A numerical analysis of chaos in the double pendulum. *Chaos, Solitions and Fractals*, (29):417–422, 2006.